JGR Oceans

RESEARCH ARTICLE

10.1029/2025JC022713

Modulation of the Ocean Surface Skin Temperature and Heat Flux in the Presence of Strong SST Fronts

Sandra L. Castro[1], **Gary A. Wick**[2], **and Andrew T. Jessup**[3]

[1]Colorado Center for Astrodynamics Research, University of Colorado, Boulder, CO, USA, [2]NOAA Physical Sciences Laboratory, Boulder, CO, USA, [3]Applied Physics Laboratory, University of Washington, Seattle, WA, USA

Key Points:

- Positive correlations between the heat flux and *SST* variability imply ocean forcing of air-sea interactions over a sub-mesoscale front
- Cross-frontal variations in heat flux better characterize the modulation of the cool skin effect across the front than the wind speed
- Use of subsurface *SST* in the COARE algorithm produced similar accuracy flux estimates to those using direct skin SST observations

Correspondence to:

S. L. Castro,
sandrac@colorado.edu

Citation:

Castro, S. L., Wick, G. A., & Jessup, A. T. (2025). Modulation of the ocean surface skin temperature and heat flux in the presence of strong SST fronts. *Journal of Geophysical Research: Oceans*, *130*, e2025JC022713. https://doi.org/10.1029/2025JC022713

Received 3 APR 2025
Accepted 27 NOV 2025

Author Contributions:

Conceptualization: Sandra L. Castro, Gary A. Wick
Data curation: Sandra L. Castro, Andrew T. Jessup
Formal analysis: Sandra L. Castro, Gary A. Wick
Investigation: Sandra L. Castro, Andrew T. Jessup
Methodology: Sandra L. Castro, Gary A. Wick, Andrew T. Jessup
Software: Sandra L. Castro
Visualization: Sandra L. Castro
Writing – original draft: Sandra L. Castro
Writing – review & editing: Sandra L. Castro, Gary A. Wick, Andrew T. Jessup

Abstract Previous studies of air-sea interactions over sharp oceanic fronts have suggested that it is the ocean that drives the atmosphere across sub-mesoscale ocean fronts, but it is the atmosphere that drives the ocean at synoptic scales; the responsible mechanism, however, is still a matter of debate. This paper examines direct sea surface temperature (*SST*) measurements of the skin (SST_{skin}) and near-surface *SST* (SST_{depth}), and wind speeds measured during the Sub-Mesoscale Ocean Dynamics Experiment (S-MODE) along with derived bulk fluxes. We evaluate the modulation of the net heat flux, wind speed, and skin cooling across *SST* fronts and the ability of the COARE bulk flux algorithm to reproduce this variability. Bulk flux computations can be performed directly from a radiometric SST_{skin}, or more commonly, from the SST_{depth} provided that the depth of the *SST* measurement is corrected for cool skin and diurnal warming effects. Both types of *SST* were measured during S-MODE allowing for (a) an assessment of the importance of having a SST_{skin} for a direct flux evaluation in frontal regions, and (b) an evaluation of the accuracy of the cool skin and diurnal warming corrections within COARE for the indirect bulk flux computation. The ocean-atmosphere feedback over the sampled S-MODE submesoscale front suggested that the ocean was indeed forcing the atmosphere, mainly through the surface net heat losses, while the wind response to changes in SST_{skin} was irregular. Testing of the COARE algorithm suggested that indirect bulk fluxes had sufficient accuracy to close the heat budget over the front.

Plain Language Summary While previous studies of air-sea interactions over oceanic fronts have suggested that it is the ocean that drives the atmosphere across sub-mesoscale ocean fronts, but the atmosphere that drives the ocean at basin scales, the ultimate mechanism is not absolutely certain. In this paper, we look at the response of the heat flux, wind speed, and cooling at the ocean surface to changes in sea surface temperature across a strong thermal front. The observed feedback suggests that it is the heat flux from the ocean to the atmosphere that dominates the air-sea feedback over the sub-mesoscale front. We then use one of the most popular models to compute heat fluxes over the ocean, the so-called COARE bulk flux algorithm, to evaluate the skill of the model in estimating fluxes over the front. Because the ocean temperature changes with depth, the COARE model can be run using radiometric temperatures, which are more direct but challenging/expensive or deeper temperatures that are easier/cheaper to measure but require additional corrections to account for the shape of the ocean surface temperature profile and can introduce errors. Results indicate that the simpler measurements are good enough to evaluate the fluxes over the front.

1. Introduction

The ocean's impact on weather and climate is determined by processes near the ocean's surface. A complex interaction of mesoscale weather-related processes such as wind, rain, the daily heating and nightly cooling of the ocean, and changes in sea surface temperature (*SST*) and humidity contribute to the mixing of the upper ocean. At large basin scales, wind intensification is primarily responsible for the cooling of the ocean surface through evaporation. Wind is also a contributing factor in the entrainment of cool surface water deeper into the mixed layer. Thus, mixing of the upper ocean at large scales is predominantly forced by the atmosphere. The ability of the atmosphere to modify the ocean surface depends on the rate at which heat and momentum can be transported across the air-sea interface (Moum & Smith, 2019).

Over smaller mesoscale and submesoscale features, however, the cooling of the upper ocean is predominantly forced by the ocean through the net upward heat flux at the air-sea interface (Small et al., 2008). Heat is lost to the atmosphere at the surface by longwave radiation, evaporative cooling and conduction. Local mixing can also occur through frontal instabilities, a phenomenon associated with submesoscale fronts. Baroclinic instabilities of

upper ocean fronts generate submesoscale eddies that lead to rapid restratification of the mixed layer on a time scale of a few days and a length scale of 1–10 km (Fox-Kemper et al., 2008; Hosegood, 2006; Mahadevan et al., 2010). Restratification by submesoscale mixed-layer eddies results from the eddy-driven thermal overturning circulations that convert horizontal density gradients to the vertical. The wind can enhance or inhibit the mixed layer eddy restratification depending on the relative orientation of the wind with respect to the front. If there is alignment and the wind stress has a down-front component, the restratification by mixed layer eddies is halted by the transport of buoyancy induced by the down-front wind stress acting in the direction of the geostrophic velocity. This process ultimately leads to intensification or persistence of the upper ocean front (e.g., Thomas & Ferrari, 2008). If, however, the wind is not aligned with the frontal axis, frontal (baroclinic) instabilities can grow, giving rise to eddies able to dominate over the wind forces that act quickly to restratify the mixed layer.

The focus of the Sub-Mesoscale Ocean Dynamics Experiment (S-MODE), a NASA project consisting of a series of field campaigns from 2021 to 2023, was understanding the physics of submesoscale fronts and eddies and their effect on vertical transport in the upper ocean. The data utilized here were collected during the first intensive operating period (IOP-1), which consisted of repeatedly sampling a sharp and persistent submesoscale thermal front off the coast of San Francisco in 2022. This paper examines differences in the vertical interfacial exchange across the front in terms of variability among the measured *SST*, skin layer cooling, and wind speed, and model-derived heat fluxes, as well as the ability of existing models to reproduce the changes. It addresses the primary mechanism driving the stratification of the surface mixed layer when there is a sharp submesoscale thermal front present.

The typical net upward heat flux at the surface of the ocean results in a cool skin layer of $O(1\text{ mm})$ thick (Saunders, 1967). The temperature at the top of this layer, known as the skin temperature SST_{skin}, can be up to 0.5 K cooler than the temperature directly below, known as the subskin temperature SST_{subskin}. The presence of a cool skin layer influences the exchange of heat and gas across the air-sea interface and is relevant to satellite *SST* products. The relatively rare circumstance of a net downward heat flux results in a warm skin layer, which has been recently reported as being more common than previously thought (Jia & Minnett, 2023; Zhang et al., 2020).

Figure 1 illustrates the typical upper ocean thermal structure when a cool skin is present under nighttime and daytime conditions. At night, the temperature below the skin layer is well mixed, while during the day a diurnal warm layer can occur due to solar heating. We define the temperature difference across the skin layer as $\Delta T_{\text{skin}} = SST_{\text{skin}} - SST_{\text{subskin}}$, which is negative for a cool skin and positive for a warm skin. Diurnal warming can cause SST_{subskin} to be several degrees warmer than the temperature of the water column at a greater depth, designated as SST_{depth}. We define the temperature difference across the diurnal warm layer as that between the subskin and an arbitrary depth to be $\Delta T_{DWL} = SST_{\text{subskin}} - SST_{\text{depth}}$. The temperature difference between the skin and an arbitrary depth is defined as $\Delta T_{\text{depth}} = SST_{\text{skin}} - SST_{\text{depth}}$. In general, $SST_{\text{skin}} = SST_{\text{depth}} + \Delta T_{DWL} + \Delta T_{\text{skin}}$. Table 1 summarizes the nomenclature and definitions for the quantities describing the near-surface temperature profiles and relevant differences.

An extensive amount of theoretical work exists on modeling and predicting ΔT_{skin} (see comprehensive reviews by Katsaros (1980), Robinson et al. (1984), Wick et al. (1996) and Castro et al. (2003)). Early work generally follows Saunders (1967), who predicted that ΔT_{skin} is given by

$$\Delta T_{\text{skin}} = \lambda \frac{\nu Q_{\text{net}}}{k u_*}, \tag{1}$$

where Q_{net} is the net heat flux at the surface, u^* is the friction velocity in the water, k is thermal conductivity of seawater and λ is a proportionality coefficient. According to (Equation 1), ΔT_{skin} depends on both the net heat flux and the wind speed via u^*. An alternative approach was developed within the context of surface renewal theory, which assumes that the skin layer is constantly being disrupted and replaced with water from below (e.g., Jessup et al., 2009; Kudryavtsev & Luchnik, 1979; Kudryavtsev & Soloviev, 1981; Kudryavtsev & Soloviev, 1985; Liu & Businger, 1975).

The cool skin effect has also been empirically parameterized based solely on either the wind speed, U, or the difference between the saturation specific humidity at the surface, q_s, and the specific humidity in the air above, q_a. With respect to U, Donlon et al. (1999) proposed that for nighttime conditions:

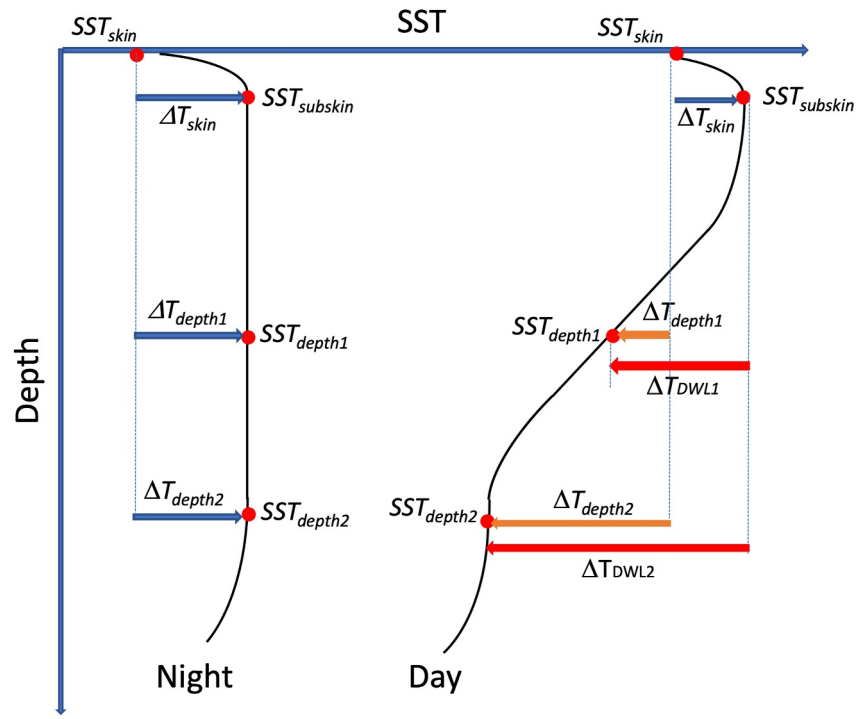

Figure 1. Idealized temperature profiles of the oceanic near-surface layer for nighttime (left) and daytime conditions (right). Colored arrows indicate different definitions of ΔT according to the depth of the measurements: blue for ΔT_{skin}, orange for ΔT_{depth}, and red for ΔT_{DWL}. See Table 1 for definitions.

$$\Delta T_{\text{depth}} = -0.30 \exp(-0.27\ U) - 0.14, \tag{2}$$

which has been interpreted to represent the average cool skin effect at night, when $\Delta T_{\text{skin}} \approx \Delta T_{\text{depth}}$. Donlon et al. (2002) subsequently found that ΔT_{depth} at wind speeds above ~6 m s^{-1} tended to a mean value of approximately −0.17 K and proposed to further simplify (Equation 2) to $\Delta T_{\text{skin}} \approx \Delta T_{\text{depth}} = -0.17$ K for $U > 6$ m s^{-1}, for both day and night. Several similar $\Delta T_{\text{depth}} = f(U)$ parameterizations have since been reported for a wide range of conditions (e.g., Jia et al., 2023; Minnett et al., 2011; Yang et al., 2023; Zhang et al., 2020). While these results show significant scatter in the ΔT_{depth} observations around (Equation 2), wind speed parameterizations avoid issues such as the availability of, or uncertainty in, the heat flux measurements, permitting a straightforward estimation of a mean ΔT_{skin}. With respect to $\Delta q = q_s - q_a$, Yan et al. (2024) proposed an alternate empirical model based on a fit to the theoretical Coupled Ocean-Atmosphere Response Experiment (COARE) cool skin model (Fairall, Bradley, Godfrey, et al., 1996) in the tropics, where the latent heat flux is the largest contributor to the heat loss across the cool skin:

$$\Delta T_{\text{skin}} = a\ \Delta q + b, \tag{3}$$

where $a = -3.498 \times 10^{-2}$, $b = -3.851 \times 10^{-2}$, and ΔT_{skin} is given in K when Δq is in units of g kg^{-1}. Unique S-MODE observations provide the opportunity to assess the suitability of these simplifications in the vicinity of strong temperature fronts and associated changes to the heat flux.

The variability of the near-surface temperature due to the combination of the cool skin and warm layer effects impacts methods to estimate the air-sea heat flux. According to Fairall, Bradley, Godfrey, et al. (1996), estimating the heat balance to an accuracy of 10 W m^{-2} requires specification of the *SST* to an accuracy of ±0.2 K. SST_{skin} is the appropriate *SST* for heat flux computations because it best represents the temperature at the air-sea interface. When SST_{depth} is the only available *SST*, it can be converted to SST_{skin} using parameterizations or models of the cool skin and warm layer effects, such as those in the COARE bulk flux algorithm (Fairall, Bradley, Rogers, et al., 1996).

Table 1
Definitions

Parameter	Definition	Description/Note
Temperature		
SST	Sea Surface Temperature	Near surface temperature with no depth reference
SST_{skin}	Skin Temperature	SST at the air-sea interface
$SST_{subskin}$	Subskin Temperature	SST at the base of the skin layer
SST_{depth}	Bulk Temperature	SST at depth, here measured by the sea snake at ∼5 cm
T_w	Water Temperature	SST_{skin}, used for the sea-air temperature difference
T_a	Air Temperature	Temperature from ASIMET anemometer at 15.25 m
Heat Flux		
Q_{net}	Net Heat Flux	$Q_{net} = Q_{LW\text{-}net} + Q_E + Q_H$
$Q_{LW\text{-}net}$	Net Longwave Flux	$Q_{LW\text{-}net} = Q_{LW\text{-}down} - Q_{LW\text{-}up}$
Q_E	Latent Heat Flux	
Q_H	Sensible Heat Flux	
Q_{net}, SST_{skin}	Q_{net} using SST_{skin}	
Q_{net}, SST_{depth}	Q_{net} using SST_{depth}	
Temperature Differences		
ΔT_{skin}	SST_{skin}—$SST_{subskin}$	Temperature difference across skin layer. Negative for a cool skin, positive for warm skin
ΔT_{DWL}	$SST_{subskin}$—SST_{depth}	Temperature difference across the diurnal warm layer
ΔT_{depth}	SST_{skin}—SST_{depth}	Temperature difference between the skin and at depth
T_w–T_a	SST_{skin}—T_a	Sea-Air Temp. Diff. >0: unstable atm.; <0: stable atm.
Cross-Frontal Differences		
ΔSST_{skin}		Along-track |Max–Min| Difference in SST_{skin}
ΔQ_{net}		Along-track |Max–Min| Difference in Q_{net}
ΔU		Along-track |Max–Min| Difference in U
$\Delta(\Delta T_{skin})$		Along-track |Max–Min| Difference in ΔT_{skin}
$\Delta(T_w$–$T_a)$		Along track difference in T_w–T_a for max (SST_{skin}) and min (SST_{skin})

Here we use COARE to estimate the net heat flux in our analysis and also use our measurements of SST_{skin} to evaluate the skill of COARE to predict ΔT_{skin}. We present the results of three different analyses:

1. Analysis of the modulation of the heat flux, wind speed and ΔT_{skin} in response to changes in the cross-frontal variability of the SST_{skin};
2. Characterization of the spatial variability of a submesoscale SST front with horizontal length scale based on a statistical self-similarity analysis, and
3. A sensitivity study of the net heat flux estimates in the presence of a sharp thermal front using COARE with different SST inputs and ΔT_{skin} parameterizations.

The differences between SST_{skin}- and SST_{depth}-derived fluxes are evaluated and used to further quantify potential uncertainties in the heat flux computation resulting from forcing the COARE algorithm with SST_{depth}. We also compare the observed ΔT_{depth} to both the COARE ΔT_{skin} and the simplified parameterizations in Equations 2 and 3.

2. S-MODE IOP-1 Data

The satellite SST image of the S-MODE IOP-1 study area in Figure 2 shows the persistent front and the ship tracks for the entire experiment. Subsequent satellite imagery showed that the front persisted for over 2 weeks with little change in orientation and magnitude. The *in situ* data were collected aboard the M/V *Bold Horizon* and are

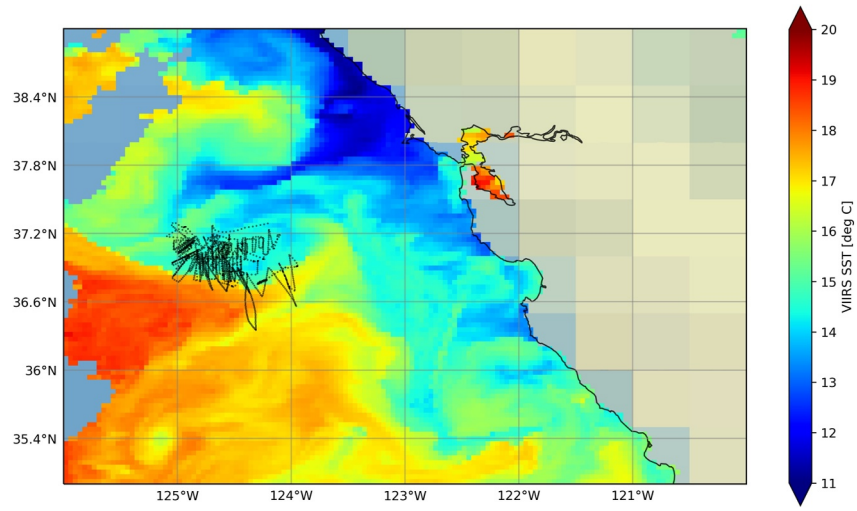

Figure 2. Geographical domain of the NASA S-MODE IOP1 experiment, with ship tracks from M/V *Bold Horizon* from 11 to 24 October 2022. The background VIIRS (Visible Infrared Imaging Radiometer Suite) *SST* image, corresponding to 24 October 2022, shows the thermal front, which was the focus of this field campaign. The front persisted, and remained stationary, for over 2 weeks.

summarized in Table 2, with the derived flux parameters listed in Table 3. All instrument outputs were sampled at 1 Hz and averaged to a period of 1 min except SST_{skin}, which was provided at an interval of approximately 5 min.

2.1. Meteorological Measurements

Meteorological instruments used were the ASIMET package (Air-Sea Interaction METeorology, Woods Hole Oceanographic Institution), a WS-501-UMB Smart Weather Sensor and a SGR3-V Smart Pyrgeometer (OTT Hydromet). The ASIMET system was installed on the ship's mast at 15.25 m above the surface and the WS-501 and SGR3-V were installed at 12.2 m on the port side of the upper deck. Due to technical difficulties outlined in Appendix A, wind speed and direction were derived using the ASIMET package, supplemented by the wind sensor in the WS-501. Downwelling longwave radiation was provided by the SGR3-V. Measurement time series were visually examined for basic quality screening.

2.2. Sea Surface Temperature

The *SST* observations included radiometric measurement of SST_{skin} and contact measurement of very near-surface SST_{depth}.

SST_{skin} was derived using radiometric measurements from two identical Remote Ocean Radiometer Systems (ROSR), denoted by their serial numbers as ROSR3 and ROSR9. ROSR is a commercially manufactured system (RMR, Co., defunct) that is comparable in design and performance to the Infrared Sea surface temperature Autonomous Radiometer (ISAR, Donlon et al., 2008). Two ROSRs were deployed in order to assess

Table 2
Properties of Measured Quantities

Measured quantity	Sensor	Samp. Rate	Accuracy	Note
SST_{skin}	ROSR	1/5 min	±0.10 K	
SST_{depth}	SBE-39	1 Hz	±0.002 K	Acc. Range: −5 to +35°C
Wind Spd (U) and Dir.	ASIMET	1 Hz	1%, 3°	R.M. Young 5103 and WS-501
Air Temp. (T_a)	ASIMET	1 Hz	0.05 K	Rotronic MP-101A
Rel. Hum. (RH)	WS-501	1 Hz	±2%	
LW down (LW_{down})	SGR3-V	1 Hz	5%	

Table 3
Properties of Derived Quantities

Derived quantity	Measurements used	Source
Latent Heat Flux	RH, T_a, SST_{skin}, U	COARE bulk formula
Sensible Heat Flux	T_a, SST_{skin}, U	COARE bulk formula
Net LW radiation	LW_{down}, SST_{skin}	COARE uses LW_{up} via Stefan-Boltzman
Net SW radiation	SW_{down}	COARE with integrated emissivity value

measurement uncertainty, which was demonstrated to be ±0.10 K (Jessup, 2025). The data from ROSR9 are used here because it had fewer data gaps than ROSR3. ROSR provides a SST_{skin} retrieval approximately every 5 min. During this period, the radiometer is sampled at 0.5 Hz and uses averaged values over sequential views of the sea surface for 80 s, the sky for 20 s, and two internal calibration blackbodies for 20 s each to produce a single SST_{skin} value.

Measurements of SST_{depth} were made using a buoyant, surface trailing thermistor, known as a sea snake, which consisted of a SBE-39 thermistor (SeaBird) installed at the end of a 50-ft long Tygon tube. The sea snake was deployed in the wake from a 3-m boom extending out from the side of the ship. Similar incarnations have been deployed with the assumption that its shallow measurement of SST_{depth} is a good estimate of $SST_{subskin}$ in the absence of significant diurnal warming, with an estimated measurement depth of 5 cm (Fairall et al., 1997). In Appendix B we use diurnal warm layer models to evaluate the use of the sea snake measurement and conclude that it provided a good estimate of $SST_{subskin}$ at all times of day during IOP-1 due to the absence of significant diurnal warming.

2.3. Heat Fluxes

The net heat flux was computed as $Q_{net} = Q_{LW\text{-}net} + Q_E + Q_H$, where $Q_{LW\text{-}net}$ is the net longwave radiation and Q_E and Q_H are the latent and sensible heat fluxes, respectively. We use the convention that $Q > 0$ upward. The net shortwave radiation is not included because the fraction of shortwave radiation absorbed within the skin layer is small (e.g., Wick et al., 2005). The individual flux components were computed using the COARE bulk flux version 3.6 algorithm (Edson et al., 2013; Fairall et al., 2003). The COARE bulk fluxes were computed using both SST_{skin} derived from ROSR9 and SST_{skin} from COARE based on SST_{depth} from the sea snake. The COARE SST_{skin} computation uses the embedded ΔT_{skin} and ΔT_{DWL} parameterizations, such that COARE SST_{skin} = SST_{depth} + COARE ΔT_{skin} + COARE ΔT_{DWL}. The COARE ΔT_{skin} module uses a model based on (Equation 1), with a proportionality coefficient λ that encompasses a transition between a shear-driven and a convective-driven regime (see Equation 14 in Fairall, Bradley, Godfrey, et al., 1996). The COARE warm layer correction (Fairall, Bradley, Godfrey, et al., 1996) is based on the Price-Weller-Pinkel turbulent mixing model (Price et al., 1986).

2.4. Sampling Strategy

The ship speed was maintained at approximately 3 m s^{-1} during the frontal crossings in order to provide continuous and uniform sampling with the underway CTD. The constant ship speed and the stationarity of the front allows us to use time series analysis to evaluate the cross-frontal parameters. All variables used in the analysis were resampled to 10-min resolution to be consistent with the 5-min SST_{skin} data rate from the ROSR and to avoid any additional uncertainties associated with application of the bulk heat flux method on shorter time scales in the presence of strong gradients.

3. Results

Time series of SST_{skin}, U, Q_{net}, and ΔT_{skin} are shown in Figure 3 for the entire IOP-1. The SST_{skin} shows remarkably large and consistent temperature differences of ∼4°C between the warm and cool side of the front. A relatively high wind speed of ∼8 m s^{-1} persisted for most of IOP-1, with the exception of the short period between Day of Year (DOY) 288–292 (15–19 October) when the wind speed was ∼2–4 m s^{-1}. The net heat flux (here based on the measured SST_{skin}) and ΔT_{skin} time series both show strong modulations that appear highly correlated with the cross-front SST_{skin}.

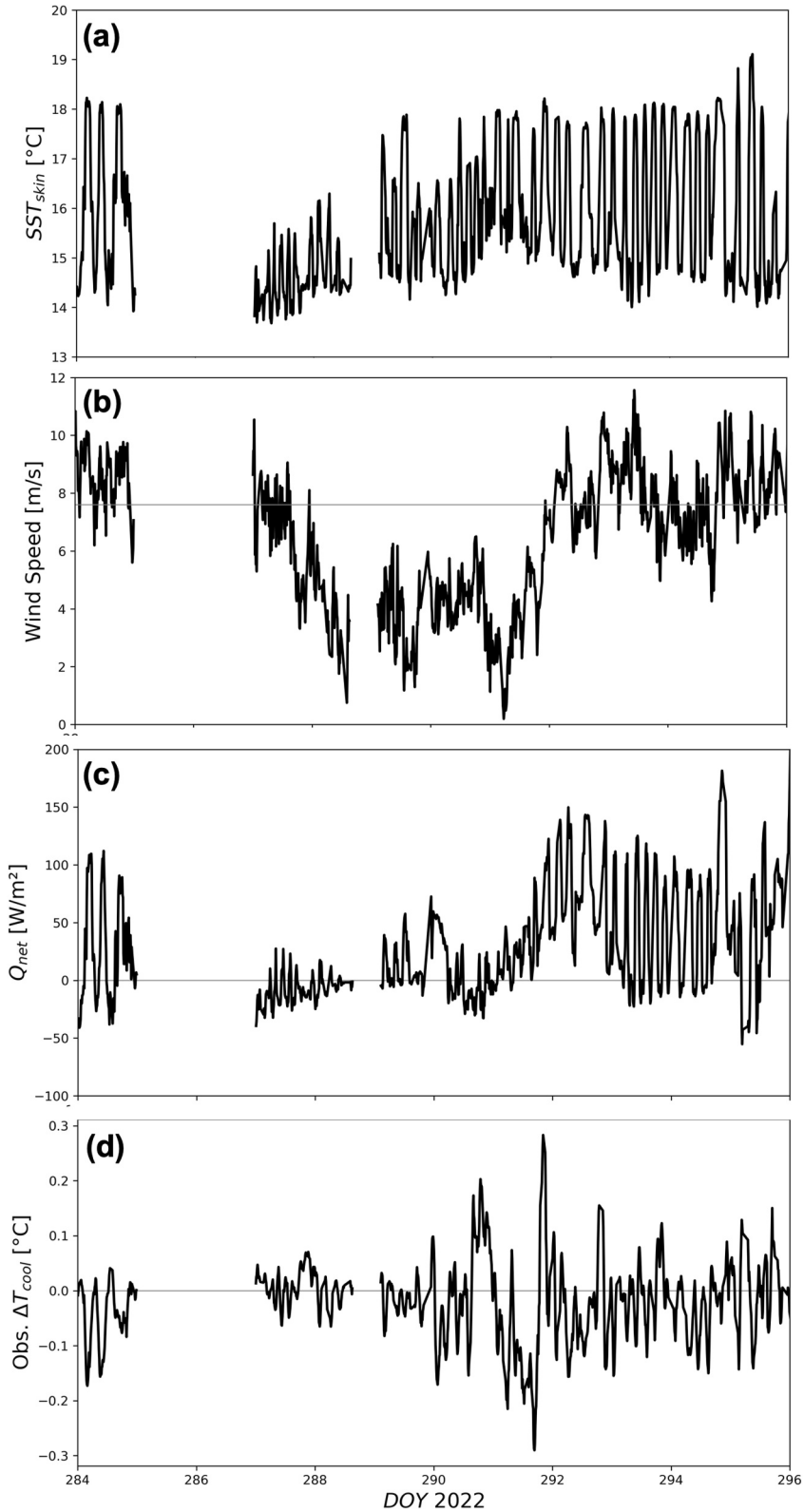

Figure 3. Time series, from DOY 284–296 (11–24 October 2022) of (a) the skin temperature SST_{skin}, (b) the wind speed U, (c) the net heat flux Q_{net}, and (d) the observed cool skin ΔT_{skin}. The missing data from DOY 285–287 are due to an unplanned port visit.

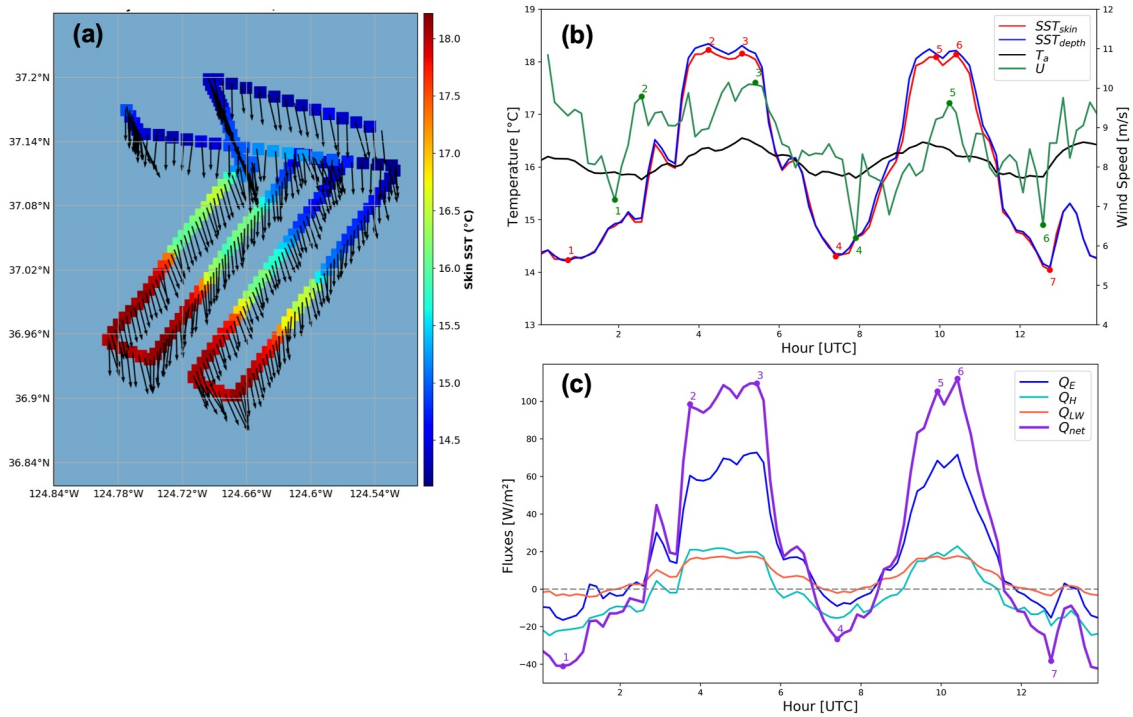

Figure 4. Comparisons for DOY 284 (11 October 2022) between 0000 UTC and 1400 UTC (a) ship track color-coded by SST_{skin} with vector winds, (b) time series of (left-axis) temperatures SST_{skin}, SST_{depth}, T_a and (right-axis) wind speed U, and (c) time series of heat flux components: net longwave radiation, Q_{LW}, latent flux, Q_E, and sensible flux, Q_H. The net heat flux Q_{net} is shown in purple. Measurements after 0200 UTC corresponded to local nighttime.

3.1. Detailed Example of Cross-Frontal Modulation

The observations on DOY 284, shown in Figure 4, provide a striking example of strong cross-frontal modulation. The ship track in Figure 4a, tagged with wind vectors and color coded by SST_{skin}, shows that the transects were roughly perpendicular to the front and that the wind conditions were relatively constant. The time series in Figure 4b show that SST_{skin} changed by as much as 4°C and that the modulation of the air temperature, T_a, across the front was less than 1°C. We use the sea-minus-air temperature difference, denoted here as T_w–T_a, and computed as $SST_{skin} - T_a$, to characterize the atmospheric stability and help understand the air-sea interactions across the front. Positive differences (sea warmer than overlaying air) correspond to an unstable atmosphere and a negative difference (air warmer than sea) indicates a stable atmosphere. According to Figure 4b, T_a was cooler than SST_{skin} on the warm side of the front and warmer than SST_{skin} on the cool side. The change in sign of T_w–T_a along the transects indicates that there was a change in near-surface stability across the front, from unstable conditions on the warm side to stable conditions on the cool side. The sea snake measurement, SST_{depth}, is significantly greater than SST_{skin} on the warm side of the front, which indicates the presence of a strong cool skin layer. The lack of a noticeable difference between the SST_{skin} and SST_{depth} on the cool side indicates a weak skin. The fluxes in Figure 4c show positive components and net heat fluxes on the warm side, with Q_{net} ~100 W m^{-2}, Q_E increasing rapidly up to ~60 W m^{-2}, and Q_H at ~ 20 W m^{-2}. The cool side shows small negative component and net fluxes, with Q_{net} ~ −20 to −40 W m^{-2}, Q_E ~ 0 and Q_H ~ −20 W m^{-2}. The occurrence of a negative latent heat flux corresponds to condensation on the ocean surface as opposed to evaporation.

The wind vectors show no clear evidence of a strong response to the changes in SST and stability across the front. Figures 4b and 4c indicate that the wind speed increased in phase with both SST_{skin} and the heat flux only for cases of $Q_{net} > 0$ W m^{-2}, on the warm side of the front. For $Q_{net} < 0$ W m^{-2}, the wind speeds appear to be anticorrelated with the fluxes. As the ship starts to traverse the front from the cool to the warm side, the wind speed tends to decrease as Q_{net} starts to increase from its minimum negative value at the start of the transect. A wind speed modulation of ~1–1.5 m s^{-1} over the warm side from an average wind speed of 7 m s^{-1} over the cold side is relatively modest compared to the strong heat flux modulation. For this period, the correlation between SST_{skin}

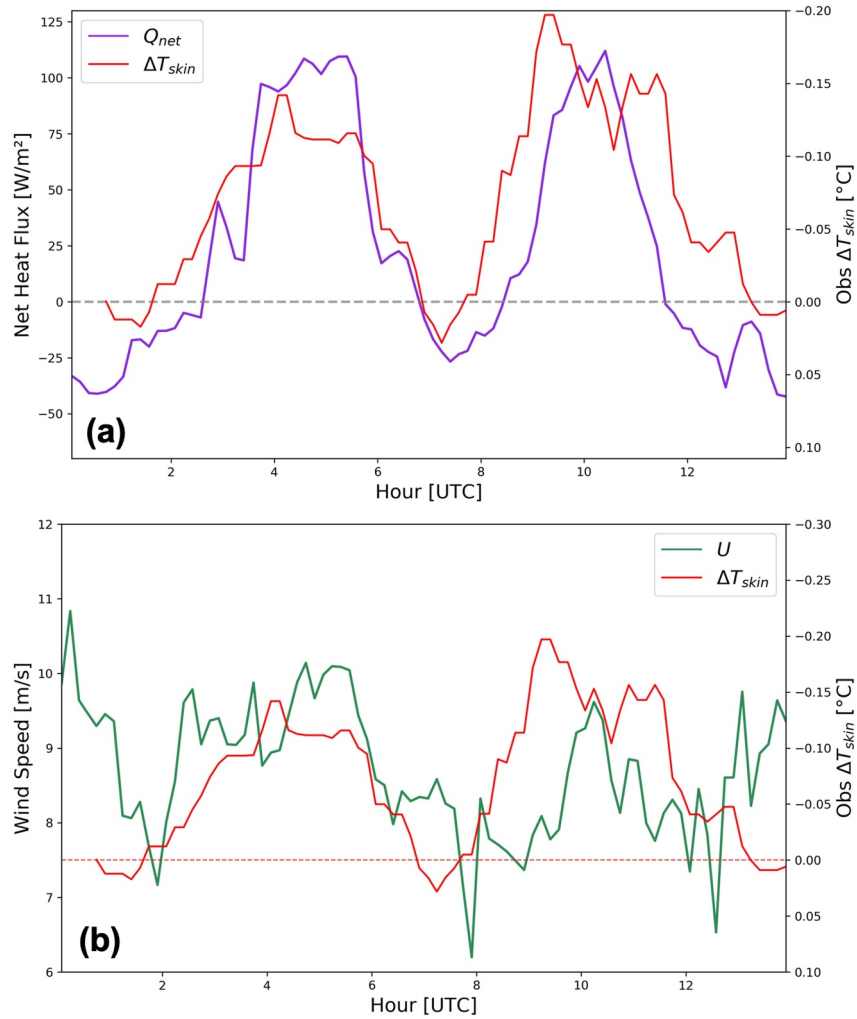

Figure 5. ΔT_{skin} time series (right axis) comparisons for DOY 284 (11 October 2022) between 0000 UTC and 1400 UTC compared to (a) time series of net heat flux Q_{net} (left axis) and (b) wind speed U (left axis). The ΔT_{skin} axis has been inverted to emphasize visual correlations with the variable on the opposite vertical axis.

and Q_{net} was 0.99, while the correlation between SST_{skin} and U was 0.35. In comparison, the correlation between SST_{skin} and Q_{net} for the entire experiment was 0.43, while the correlation between SST_{skin} and U was −0.05.

The modulation of Q_{net} and U is compared to that of ΔT_{skin} in Figure 5. The temperature scale has been inverted in Figure 5a to more clearly illustrate the positive correlation between Q_{net} and ΔT_{skin}. The ΔT_{skin} values in the plot have additionally been smoothed over a window of ±1 hr to highlight the large-scale correlation (all other analyses use non-smoothed data). For outward heat fluxes, ΔT_{skin} reaches a maximum magnitude of ∼−0.15 to −0.18°C, while it is nearly zero for downward fluxes. Increases in the outgoing heat flux generally correspond to increases in the magnitude of skin layer cooling despite some small differences in phase and the timing of sign changes. In contrast, Figure 5b shows less correlation between ΔT_{skin} and the wind speed and the changes to the wind speed are relatively small.

This example suggests two distinct patterns of heat transfer and atmospheric stability under the conditions of relatively steady U and uniform T_a across the front. On the warm side, the unstable sea-air temperature differences resulted in significant net heat loss (increased Q_{net} in excess of 100 W m^{-2}), driven mainly by evaporative cooling. This enhanced heat transport on the warm side of the front is supported by a strong cool skin layer. On the cool side, there was a small net heat flux gain by the ocean of less than −50 W m^{-2} and a correspondingly weak warm skin.

3.2. Cross-Frontal Modulation Analysis

Analysis of the cross-frontal modulation for the entire IOP-1 is based on the maximum change in SST_{skin} between the end points of the transects, ΔSST_{skin}. While gradients in SST_{skin} are described in Section 3.3, ΔSST_{skin} gives a more convenient and relatable measure of the thermal front strength. This approach also avoids any dependence on the exact distance between the points and ship track. The spatial variability of Q_{net}, U, ΔT_{skin}, T_a, and T_w–T_a are analyzed by evaluating changes between their time-series extrema in relation to the SST_{skin} extrema. The method is illustrated in Figures 4b and 4c where the extrema of the time series for SST_{skin}, Q_{net}, and U are identified by numbers 1 through 6 along the crests and troughs of the two peaks shown. The differences in the values are taken between points 1 and 2, 3 and 4, 4 and 5, and 6 and 7 for the four transects shown. These data reflect the maximum amplitude of the individual responses to changes in SST_{skin}. Only Q_{net}, U, and ΔT_{skin} peaks that were visually correlated with peaks in ΔSST_{skin} were included in the cross-frontal modulation analysis and marginal differences in the lag response were allowed. Note that the Q_{net} extrema have very good correspondence with the times of the SST_{skin} extrema, whereas the times of the U extrema can show significant offsets (e.g., the points 1 and 2 of the U-time series are poorly correlated to the points 1 and 2 of the SST_{skin}-time series). This implies that the Q_{net} modulation with ΔSST_{skin}, ΔQ_{net}, could be estimated by extracting the Q_{net} values for the end points of the transect at the times of the SST_{skin} extrema (i.e., at the times of the numbers in red in Figure 4b) or at the times of their own extrema (the purple numbers in Figure 4c). For studying the U and ΔT_{skin} modulation, however, using their differences at the time of the SST_{skin} extrema is not recommended, given the lag and poor correlation between the timing of their extrema and those of SST_{skin}.

The dependence of the cross-frontal differences on ΔSST_{skin} are shown in Figure 6. For this analysis, the changes in ΔQ_{net} with ΔSST_{skin} were analyzed based on both extrema (Figures 6a and 6d). For ΔU and $\Delta(\Delta T_{skin})$, differences were only computed at the time of their own extrema (Figures 6b and 6c). The change in stability parameter T_w–T_a with front strength was also explored. Due to the auto-correlation between $\Delta(T_w–T_a)$ and ΔSST_{skin}, with $\Delta T_w \equiv \Delta SST_{skin}$, and small cross-frontal variations in T_a (e.g., Figure 4b), a strong linear dependence is observed (Figure 6e). Thus, $\Delta(T_w–T_a)$ and ΔT_a were also computed between the values corresponding in time to the SST_{skin} extrema (Figures 6e and 6f). Points are color coded by the change in atmospheric stability across the front. Stability changes are inferred from differences in the sign of T_w–T_a at the end points of the transect: np (negative to positive): blue; pn (positive to negative): red; nn (negative to negative): cyan; pp (positive to positive): green. The former two correspond to a change in stability, while the latter two indicate no change. A stability change occurs when T_a falls between the values of SST_{skin} on opposite sides of the front.

ΔQ_{net} in Figures 6a and 6d shows a strong positive correlation with ΔSST_{skin} (correlation coefficient, ρ, equals 0.87 and 0.89, respectively), at least for frontal changes in Q_{net} less than 150 W m^{-2} and frontal thermal amplitudes less than 4°C (for larger ΔQ_{net} and ΔSST_{skin}, both figures show deviations from the linear dependence). The increase in ΔQ_{net} with ΔSST_{skin} is well described by the linear least squares fit shown in Figure 6a. When the fitted line from Figure 6a is replotted on Figure 6d, it seems to demark an upper limit for the maximum ΔQ_{net} with ΔSST_{skin}. For an increase in frontal strength between 1°C and 4°C, the differential increase in ΔQ_{net} is between ∼25 and ∼140 W m^{-2}. The points for a stable boundary layer on both sides of the front (cyan), which appear clustered, correspond to weaker fronts with strength between 1°C and 2°C and $\Delta Q_{net} < \sim 50$ W m^{-2}.

The plot of ΔU versus ΔSST_{skin} in Figure 6b shows significant scatter and a slight tendency to monotonically increase with front strength. The amplitude of the ΔU increase appears to be influenced by whether or not stability changes across the front. Figure 6b suggests that T_w–T_a changes signs for $\Delta SST_{skin} \sim 2.5$°C. For weaker SST fronts with amplitude between 1 and 2.5°C and no stability change, the ΔU modulation varies between ∼2.5 and 3.0 m s^{-1}. For stronger fronts with amplitude greater than 2.5°C and change in stability, the wind modulation with front strength varies between ∼3.0 and 4.0 m s^{-1}.

The plot of $\Delta(\Delta T_{skin})$ versus ΔSST_{skin} in Figure 6c also increases monotonically with front strength but there appears to be upper and lower boundaries. The lower boundary is well-defined and corresponds to transects with consistently stable conditions across the front (cyan). The linear fit shown in Figure 6c was performed on the cluster of stable points only. These points showed strong positive correlation ($\rho = 0.94$ vs. $\rho = 0.67$ for all the data). A limit for the upper boundary (not shown) roughly follows the same slope but offset by ∼0.1°C. The bottom cluster suggests that the minimum amplitude for the ΔT_{skin} modulation with front strength occurs for stably stratified boundary layers with generally small cross-frontal wind speed changes. For an increase in front

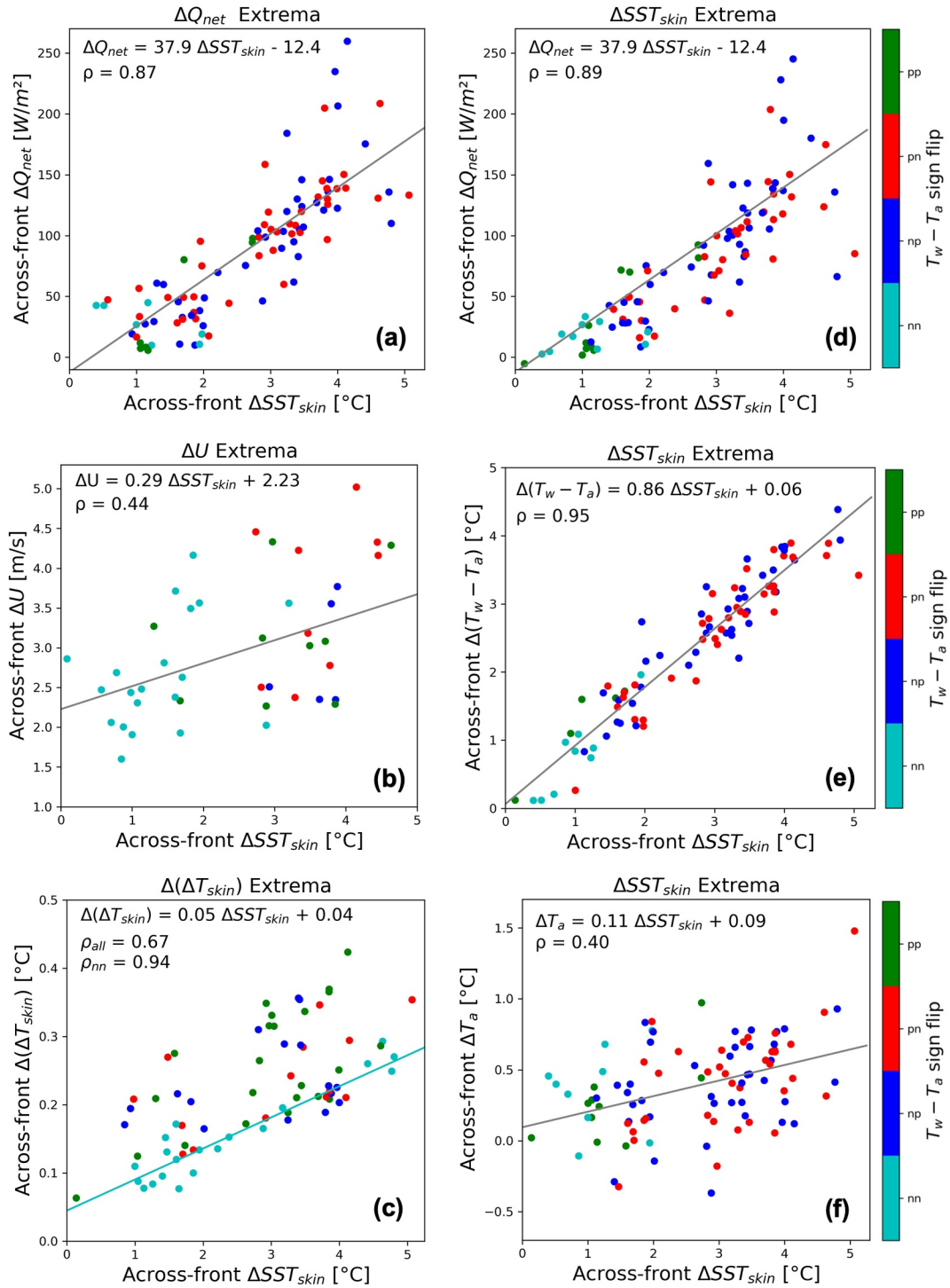

Figure 6. Cross-frontal modulations in response to changes in front strength along individual tracks, $\Delta SST_{\mathrm{skin}}$, for (a, d) the net heat flux ΔQ_{net}, (b) the wind speed ΔU, and (c) the magnitude of the skin effect $\Delta(\Delta T_{\mathrm{skin}})$, (e) the stability parameter T_w–T_a, and (f) the air temperature T_a. The $\Delta SST_{\mathrm{skin}}$ is a proxy for the strength of the front. Frontal crossings for the left column are estimated based on the extrema in the individual time series, and on the SST_{skin} extrema for the right column. The color coding corresponds to changes in the sign of T_w–T_a between the points at the ends of each transect as detailed in the text.

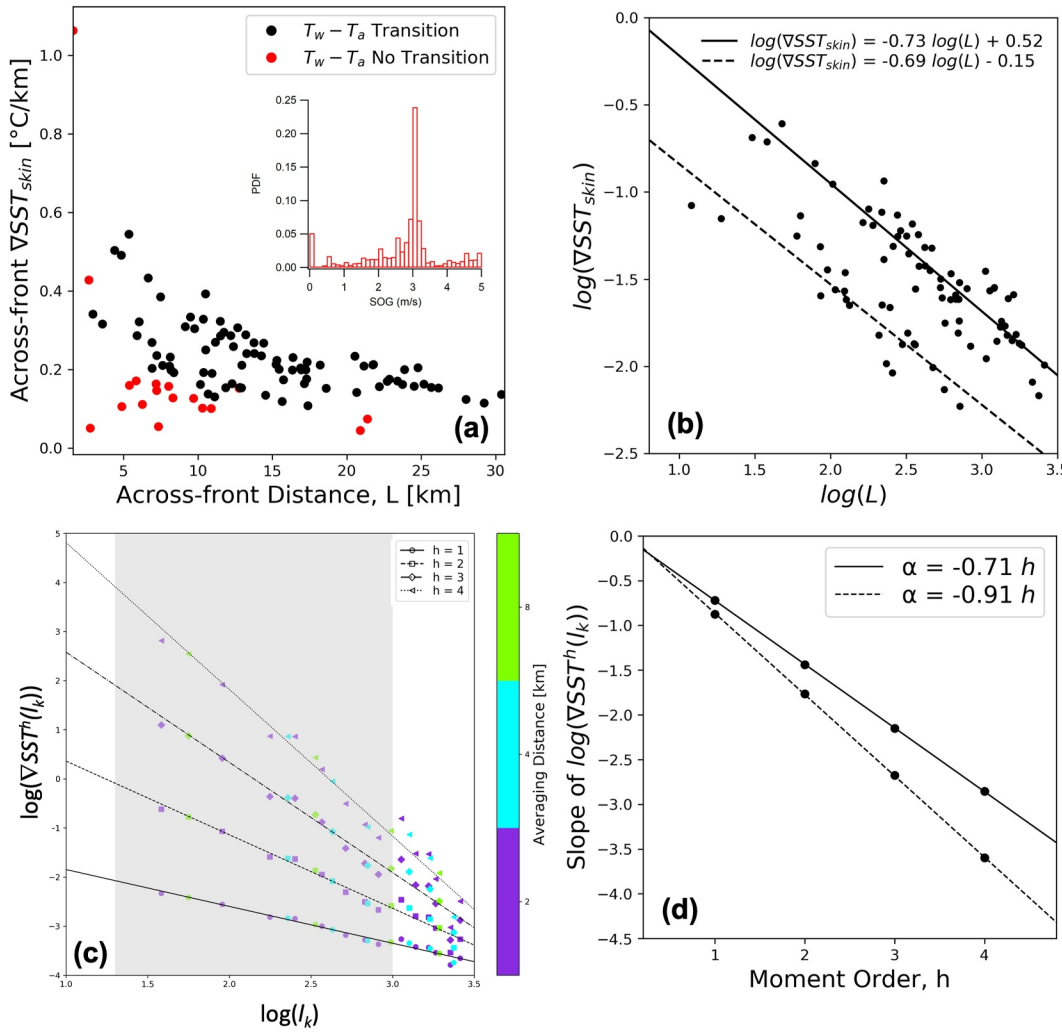

Figure 7. Examination of cross-frontal gradient magnitudes and testing for self-similarity: (a) derived gradient magnitudes, with inset ship speed histogram, (b) log-log plot of ∇SST_{skin} versus distance L, (c) testing for log-log linearity of the first four moments of the distribution of ∇SST_{skin}, and (d) testing for a linear change in slope with moment order. The color coding in panel (a) corresponds to whether the atmospheric stability changed across the front. The inset is the distribution of the ship's speed over ground (SOG) demonstrating very constant velocity during the experiment. Solid and dashed lines in panels (b, c) show results for the upper and lower grouping of points in panel (b). Colors in panel (c) correspond to the along track averaging distance and the line types indicate moment order.

strength between 1 and 5°C, the resulting increase in $\Delta(\Delta T_{\text{skin}})$ varies between ~0.1 and 0.2°C and ~0.3–0.4°C, respectively.

Despite the strong linear dependence between $\Delta(T_w – T_a)$ and ΔSST_{skin} ($\rho = 0.95$), evaluated at the SST_{skin} extrema (Figure 6e), the ΔT_a versus ΔSST_{skin} modulation (Figure 6f) is not so strongly correlated ($\rho = 0.4$). The slope of the fit of ΔT_a versus ΔSST_{skin} is 0.1 (with significant scatter) compared to a slope of 0.9 for $\Delta(T_w – T_a)$ to ΔSST_{skin}, demonstrating the modulation of the air temperature is about 10% of that of ΔSST_{skin}. Together the slopes sum to 1, corresponding to an expected one-to-one relationship for the combination of the two variables.

3.3. Self-Similarity Scaling of the Thermal Front

The spatial variability of the thermal front is characterized by the change in amplitude of the SST_{skin} gradient along the individual transects, that is, $\nabla SST_{\text{skin}} = (\max(SST_{\text{skin}}) - \min(SST_{\text{skin}}))/L$, where the SST_{skin} extrema correspond to the same transect end points identified in Section 3.2 for the modulation analysis, and L is the geographic distance between the SST_{skin} extrema. The resulting gradient amplitudes are plotted versus cross-

frontal distance L in Figure 7a. The points are color coded depending on whether the atmospheric stability changed across the front; in this case, black represents transects with change in the sign of the stability parameter T_w–T_a (previously, the np and pn colors), and red represents transects with no change in sign (previously, the nn and pp colors). The geographical distance between extrema was chosen instead of, say, the distance along the ship track because we focus on the total cross-frontal change and the ship's speed over ground (SOG) was fairly constant throughout the experiment at ∼3 m s^{-1} (see SOG histogram insert in Figure 7a). Additionally, the time series of the SST_{skin} in Figure 3a shows generally consistent temperature differences between the warm and the cool side of the front of ∼4°C, with the exception of a period during the middle of the IOP, and also fairly constant wind speed at 7.6 m s^{-1} (see Figure 3b). The persistence and homogeneity of the forcing conditions resulted in the front being quasi-stationary over the sampling period. The uniformity of sampling conditions along the transects, thus, implies that the geographical distance between the SST_{skin} extrema provides a consistent spatial framework in which the estimated gradient amplitudes are not biased by ship speed variations and frontal motions.

Gradient amplitudes (Figure 7a) ranged between 0.1 and 0.6°C km^{-1} across horizontal distances of 2–30 km, with most values occurring between $5 < L < 25$ km. The rate of decrease of the thermal front amplitude with distance suggests an exponential decay for frontal crossings with a change in stability (black points). These points also appear to be segregated into two distinct groupings, the upper curve for stronger SST gradients and lower curve for weaker gradients. Most of the IOP-1 frontal surveys fall in the upper curve. This exponential dependence between ∇SST_{skin} and L suggests statistical scaling invariance, or self-similarity.

Self-similarity over a prescribed range of scales indicates that the dominant features of the system remain similar as the scale of the system changes. This statistical symmetry under scale change is described by a "simple scaling" of the probability distributions. Proving the simple scaling hypothesis requires two conditions in the moments of the distribution (Gupta et al., 1996):

1. Log-log linearity between a specified moment and length scale, and
2. A linear change in slope $s(h) = \alpha\, h$, where h is the moment order and α is the scaling exponent.

To evaluate self-similarity for changes in thermal front amplitude with horizontal length scale, we first neglected the points that did not conform to the exponential decay of the gradient amplitude with distance in Figure 7a. These data corresponded to transects for which there was no change in the stability between the warm and cool side of the front (red points). The fact that gradients along transects with no change in cross-frontal atmospheric stability do not appear to obey the exponential decay exhibited by the fronts with a change in stability suggests that gradient similarity is contingent on the value of the air temperature being between the SST_{skin} extrema. Replotting the remaining black points on a log-log scale (Figure 7b), indicates that the points from the two exponential clusters fall on two distinct lines with fairly similar slopes, as indicated by the regression equations shown in Figure 7b. To better understand the front spatial variability, gradients from the two regimes are carried separately through the following self-similarity analysis.

To test the simple scaling hypotheses (a) and (b) stated above, we first augment the data set, artificially, by binning the gradients in Figure 7b over bins of increasing length. With each realization, we double the length of the averaging bin, starting from 1-km, to 2-, 4-, and 8-km. The first four moments (mean, variance, skewness and kurtosis) of the bin-averaged data sets are computed next. The maximum spatial averaging distance that retains the essential features of the front can be inferred when the moments of the distribution diverge from the moments of the data aggregation that preceded them. For the regime with the stronger ∇SST_{skin} (upper cluster in Figure 7b), the moments start to diverge for an averaging distance of 8 km, while for the regime with the weaker fronts this happens at 4 km. The proof of condition (a), the log-log linearity of the moments of ∇SST_{skin} with length scale, is shown in Figure 7c for the cluster with the stronger gradients. The different symbols identify different moment order, h, of the gradient distributions (circle: $h = 1$, square: $h = 2$, diamond: $h = 3$, and triangle: $h = 4$). The colors of the symbols indicate the bin size (l_k) used in binning the data across length scales: purple: 2-, cyan: 4-, and green: 8-km. The 1-km binned gradients were considered in the analysis, but are not included in the plot for clarity. The different lines correspond to linear regression fits, in log-log space, for the moments of the distributions of the different binned gradients, $\nabla SST^h_{skin}(l_k)$. It can be seen that the points representing the different moments closely follow the corresponding regression lines for length scales between ∼4 and 20 km. Outside this range, and especially for length scales greater than 20 km, the data points fall rather sharply from the fitted lines. This proves the log-log linearity of the moments of the gradient amplitude distributions, at least within the range

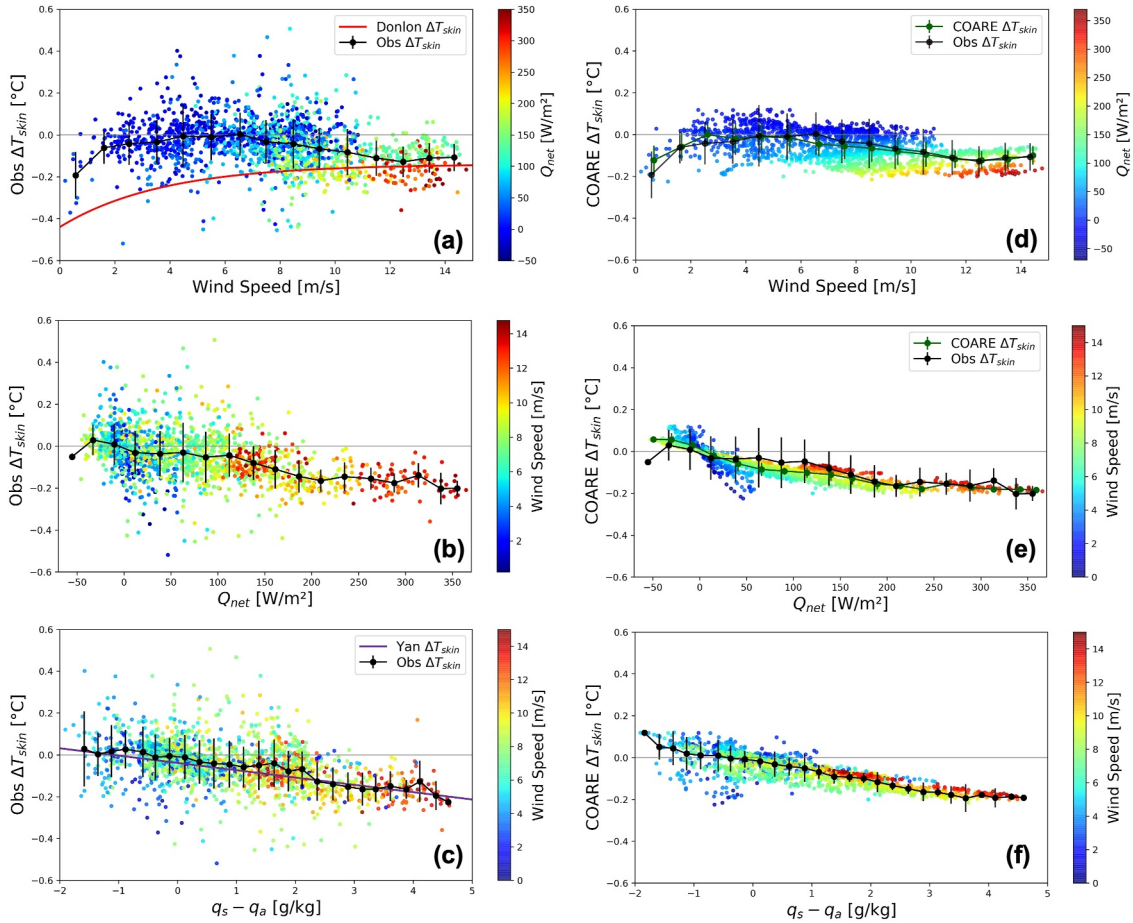

Figure 8. Dependence of ΔT_{skin} on wind speed U (top row), net heat flux Q_{net} (middle row), and the humidity difference q_s—q_a (bottom row). Left column is for the observed ΔT_{skin} and right column is for the COARE ΔT_{skin}. In panel (a) the results are compared against the wind speed $\Delta T_{\text{depth}} = f(U)$ parameterization (2), shown by the red line, and in panel (c) the results are compared against the $\Delta T_{\text{depth}} = f(q_s—q_a)$ parameterization (3), shown by the purple line. Binned error bar curves for the observed ΔT_{skin} shown in black in panels (a–c), are replicated in panels (d–f) for comparison against the green binned error bar curves for the COARE ΔT_{skin}.

of length scales highlighted by the shaded box in gray. For the regime with the weaker ∇SST_{skin} (lower cluster in Figure 7b), the log-log plot of the moments of the gradients is very similar and not shown.

Scaling condition (b), is proven in Figure 7d, as the slopes of the fitted lines from Figure 7c for the moments of ∇SST_{skin}, plotted against moment order, fall in a perfect monotonically decreasing line, $s(h) = \alpha\, h$. The slope of the solid line indicates a scaling exponent of −0.71 (i.e., $\alpha \sim -5/7$) for the strong gradient regime. In other words, this analysis supports the hypothesis that the S-MODE IOP-1 SST front obeyed statistical simple scaling, described by the power law function: $\nabla SST_{\text{skin}} \sim l^{-5/7}$, for cross-frontal distances in the 4–20 km range. The scaling exponent for the weak gradient regime, given by the slope of the dash line shown in Figure 7c, was equal to −0.91.

3.4. ΔT_{skin} Dependence on Environmental Parameters

Saunders (1967) model in (1) predicts ΔT_{skin} to be directly proportional to Q_{net} and inversely proportional to u*, which implies an inverse relationship with U. However, the dependence on heat flux and wind speed are difficult to separate analytically since Q_{net} includes the latent and sensible heat fluxes, which both depend on wind speed. The heat flux and wind speed dependence can be examined graphically by plotting ΔT_{skin} versus one parameter and color-coded by the other, and then vice versa.

The observed ΔT_{skin} is plotted versus U and color-coded by Q_{net} in Figure 8a and is plotted versus Q_{net} and color-coded by U in Figure 8b. The relatively large amount of scatter is characteristic of individual, or raw,

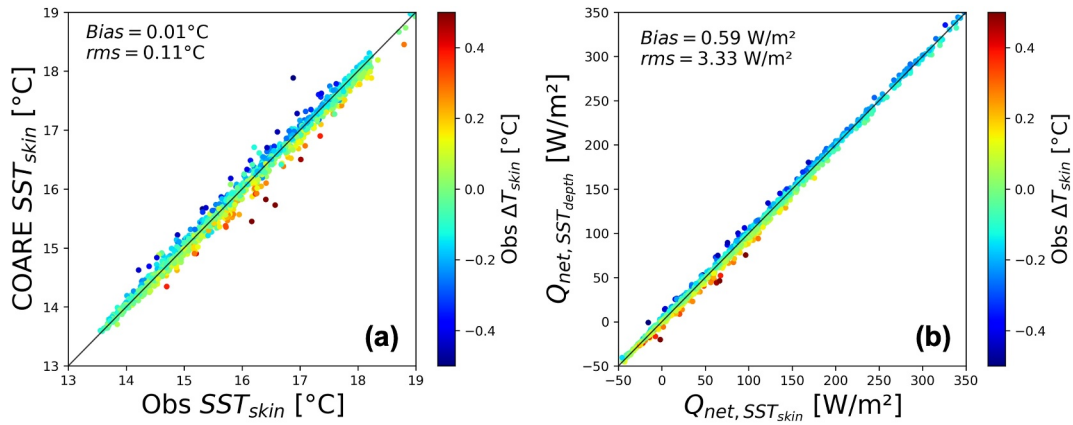

Figure 9. Scatter plots of (a) the COARE SST_{skin} versus the observed radiometric SST_{skin} and (b) the COARE Q_{net} using the observed SST_{skin}, $Q_{net,\ SST skin}$ vs. that using the COARE SST_{skin}, derived from the observed sea snake SST_{depth}, $Q_{net,\ SST depth}$.

measurements of ΔT_{skin}, which is based on SST_{skin} with an uncertainty of ±0.1 K. In practice, ΔT_{skin} is typically bin-averaged to reveal overall trends by reducing the scatter. The results of averaging over wind speed bins of 1 m s^{-1} in Figure 8a, and averaging over heat flux bins of 25 W m^{-2} in Figure 8b, are plotted over the raw data as black curves, with corresponding error bars for each bin of ± one standard deviation. The raw data show a significant number of points for which $\Delta T_{skin} > 0$ when $Q_{net} > 0$, indicating a warm skin with a net upward heat flux, which violates (1). However, the bin-averaged curve in Figure 8b shows $\Delta T_{skin} > 0$ only for $Q_{net} < 0$, indicating a physically possible warm skin under the relatively rare condition of a net downward flux. In S-MODE IOP1, a net downward flux was observed 34% of the time. For this 34%, there were consistent raw warm skin observations for 19% of the time and inconsistent raw cool skin values 15% of the time. The plot of ΔT_{skin} versus Q_{net} in Figure 8b shows a clear increase in the magnitude of ΔT_{skin} with increasing flux. The red curve in Figure 8a is the wind speed parameterization in (2). The magnitude of the observed ΔT_{skin} is comparable to that predicted by (2) only for $U > 10$ m s^{-1}, but is significantly smaller in magnitude for $0 < U < 10$ m s^{-1} where values were typically quite small.

Yan et al. (2024) assumed that the heat flux is dominated by the latent component (i.e., $Q_{net} \cong Q_E$). If it is further assumed that the drag and heat transfer coefficients are constant, then (1) may be approximated by Δq as in (3), since Q_E and u^* are proportional to U, and the complex dependence of ΔT_{skin} on the wind speed in (1) cancels out. The observed ΔT_{skin} is further plotted versus Δq and color-coded by U in Figure 8c. While there is still significant scatter, the bin-mean values show close agreement to the Yan et al. model, both in magnitude and functional form. The direct correlation between ΔT_{skin} and Δq appears stronger than with U or Q_{net}.

The COARE ΔT_{skin} estimates are similarly plotted with U, Q_{net}, and Δq in Figures 8d–8f. The black curve for the binned data of the observed ΔT_{skin} versus U in Figure 8a is duplicated in Figure 8d for comparison, while the corresponding curve for COARE is shown in green. The binned COARE ΔT_{skin} captures the observed dependence on U and Q_{net} as indicated by the agreement with the binned observations. Additionally, the color of the scatter dots for the COARE ΔT_{skin} estimates suggests stratification of the cooling with both wind speed and net heat flux, whereas the observed ΔT_{skin} dots only hint at a possible stratification with Q_{net} for $U > 10$ m s^{-1}. In Figure 8f, the relationship between the COARE ΔT_{skin} and Δq is very tight, consistent with the motivation for the development of the Yan et al. model, shown in purple.

3.5. COARE SST_{skin} Uncertainty and Associated Q_{net} Sensitivity

If only SST_{depth} measurements are available, the COARE algorithm employs the ΔT_{skin} and ΔT_{DWL} parameterizations to estimate SST_{skin} for use in computation of the heat flux components. An uncertainty in the COARE SST_{skin} may affect the surface flux computation. Since diurnal warming was negligible during IOP-1, we compute the COARE SST_{skin} using the ΔT_{skin} parameterization only and then compare the Q_{net} based on the COARE SST_{skin} to that based on the observed SST_{skin}. Though small, and not included in Q_{net}, the impact of solar radiation on the computed COARE SST_{skin} was still directly incorporated.

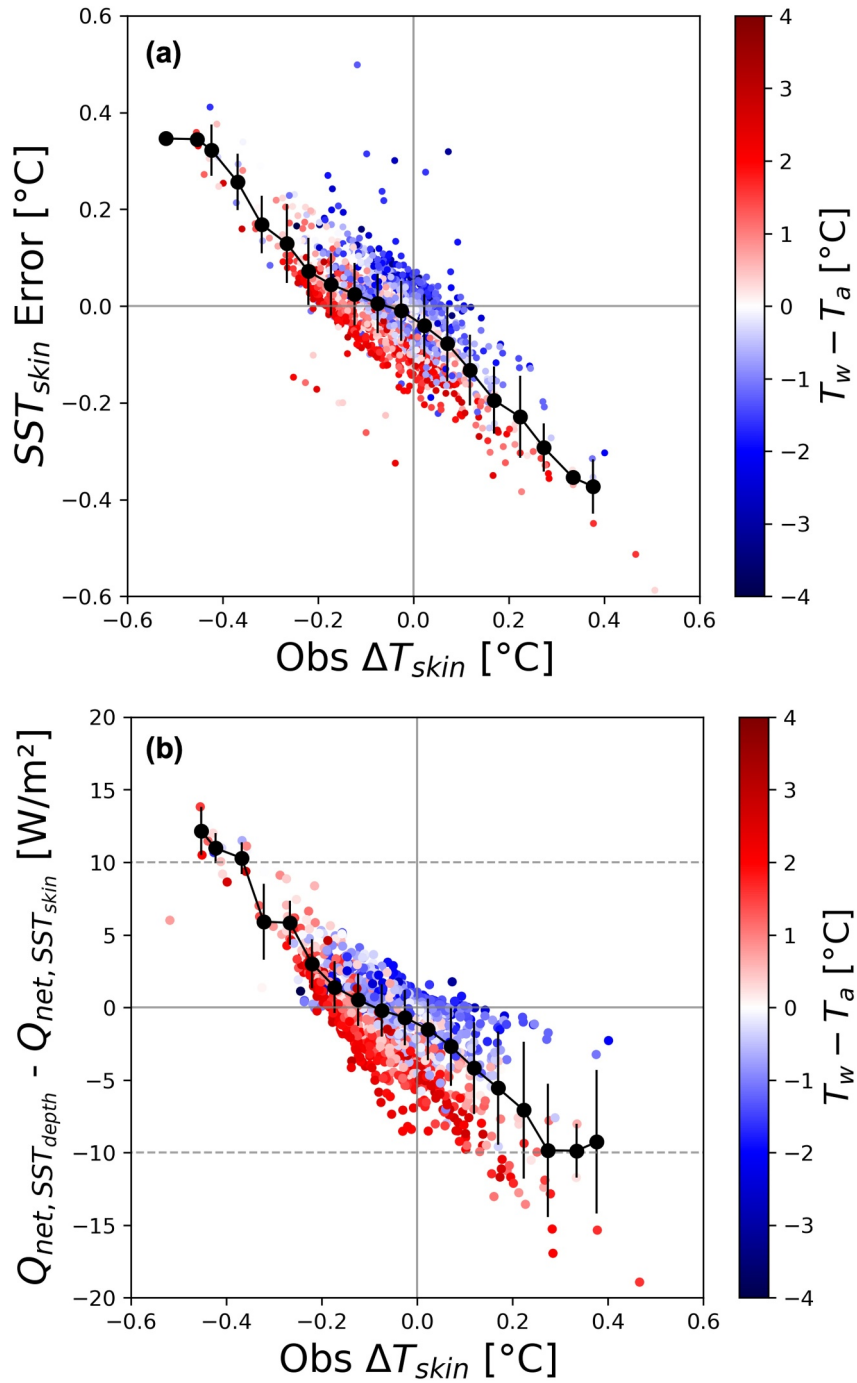

Figure 10. Scatter plots of the (a) SST_{skin} error = COARE SST_{skin}—SST_{skin} vs. ΔT_{skin} and (b) $Q_{net,\ SSTdepth}$—$Q_{net,\ SSTskin}$, versus ΔT_{skin}. $Q_{net,\ SSTdepth}$ and $Q_{net,\ SSTskin}$ denote the COARE Q_{net} estimates using SST_{depth} and SST_{skin}, respectively. The scatter plots are color-coded by the sea-air temperature difference, that is, the stability parameter, T_w–T_a.

The plot of the COARE SST_{skin} versus the observed SST_{skin} in Figure 9a shows excellent agreement, with a mean difference (bias) of 0.01°C and a root-mean-square (rms) difference of 0.11°C. The plot (Figure 9b) of Q_{net} using the observed SST_{skin}, $Q_{net,\ SSTskin}$, versus that using the sea snake SST_{depth} and the COARE skin layer correction, $Q_{net,\ SSTdepth}$, also shows excellent agreement, with a bias of 0.59 W m^{-2} and a rms of 3.33 W m^{-2}. Thus, an uncertainty in the COARE SST_{skin} of about 0.1 K translated to an overall Q_{net} difference of about 3 W m^{-2}. The results indicate that using the COARE SST_{skin} based on the sea snake SST_{depth} meets the SST accuracy requirement

that Fairall, Bradley, Godfrey, et al. (1996) concluded was necessary to estimate the heat balance to an accuracy of 10 W m^{-2}. Similar comparisons using day and night data separately yielded comparable results.

Figure 10 shows the dependence of ΔT_{skin} on differences between the COARE-estimated and observed SST_{skin} as well as on the effect of using SST_{depth} instead of the observed SST_{skin} on the computed Q_{net}. The SST_{skin} error computed as the COARE SST_{skin} minus the observed SST_{skin} is plotted versus the observed ΔT_{skin} in Figure 10a. When the observed $\Delta T_{skin} < 0$, the COARE SST_{skin} tends to be overestimated and when $\Delta T_{skin} > 0$, the COARE SST_{skin} is underestimated. This suggests that the skin effect computed by COARE is weaker than observed for both cool and warm skins. The quantity $Q_{net,\ SSTdepth}$—$Q_{net,\ SSTskin}$ plotted versus the observed ΔT_{skin} in Figure 10b, similarly shows that the difference is negative when there is a cool skin and positive when there is a warm skin. In both cases the departure is larger for a large magnitude of ΔT_{skin}.

The color coding of Figure 10 with respect to T_w–T_a shows further segregation of the COARE SST_{skin} and flux differences with atmospheric stability. For a given observed ΔT_{skin}, the COARE SST_{skin} becomes cooler as the atmosphere becomes more unstable. This is consistent with an increased outgoing flux and more skin layer cooling. If the computed SST_{skin} is underestimated relative to the observed value, however, the computed flux in COARE could be underestimated, consistent with the tendency for more negative flux differences with greater instability in Figure 10b.

The scatter plot of the COARE versus the observed ΔT_{skin} in Figure 11a demonstrates a generally strong performance of the COARE cool skin model. The results show negligible mean bias and a rms of 0.11°C. Nonetheless, there is significant scatter from the 1:1 line and the correlation coefficient ρ is 0.48. The difference statistics and correlation coefficients were similar for results considering day and night conditions separately. For comparison, the Yan et al. (2024) versus observed ΔT_{skin} scatter plot is shown in Figure 11b. The agreement is similar, consistent with the derivation of the Yan et al. model from COARE, but the correlation is slightly poorer and there is reduced ability to capture the warm skin values.

Finally, the error in the COARE ΔT_{skin} estimate, computed as COARE ΔT_{skin}—observed ΔT_{skin}, in Figures 12a and 12b shows no apparent systematic dependence on the wind speed or net heat flux. The mean errors, binned by wind speeds, show a small increase in magnitude at the lowest wind speeds (<~3 m s^{-1}) and, although there is significant scatter, the departures fall within the error bars. The mean errors binned by heat flux also suggest a small increase in magnitude near heat fluxes of ~100 W m^{-2} and below, but the differences are, again, not significant relative to the magnitude of the error bars.

4. Discussion

The results presented in Figures 7a and 7b suggested the presence of two possible SST gradient-based regimes based on the strength of the front. Furthermore, based on the criteria outlined by Gupta et al. (1996), we proved the gradients from the two regimes to obey statistical simple scaling, with scaling exponents of −0.71 and −0.91 for the strong and weak gradient regimes, respectively. A more detailed analysis of the mechanisms giving rise to the two subregimes shown in Figure 7 is beyond the scope of this paper, but, if similarity scales in the stably stratified boundary layer are an indication, these regimes are likely the result of a combination of factors involving near-surface turbulence, thermal stratification and wind shear (e.g., Sorbjan, 2010). Sorbjan (2010) proved the presence of self-similarity laws in temperature gradients for a stably stratified atmospheric boundary layer that followed a power law expressed in terms of the local stability Richardson number. He also reported four subregimes of stable turbulence controlled by different ranges of the Richardson number.

The time series of wind speed for the detailed example of cross-frontal modulation in Figure 4b showed a tendency to strengthen by 1–1.5 m s^{-1} over the warmer side from a 7-m s^{-1}-wind speed average over the cooler side. This relatively modest variation is consistent with past observations of mesoscale SST fronts (spatial scales of 100–1,000 km) showing the wind speed and wind stress being persistently stronger, by a range of 1–2 m s^{-1}, over the warmer side of the SST fronts compared to the cooler side (e.g., Chelton et al., 2007; Hayes et al., 1989; O'Neill et al., 2010, 2012; Park et al., 2006).

On the cool side of the front, the ocean was gaining heat mainly due to the air-sea temperature difference, since Q_E was negligible. The start of the frontal crossings from the detailed example occurred right after sunset and the wind speed was relatively high. Here there were no signs of oceanic stratification on the cool side despite a net downward heat flux, albeit small in magnitude, which instead resulted in a well-mixed upper ocean surface. The

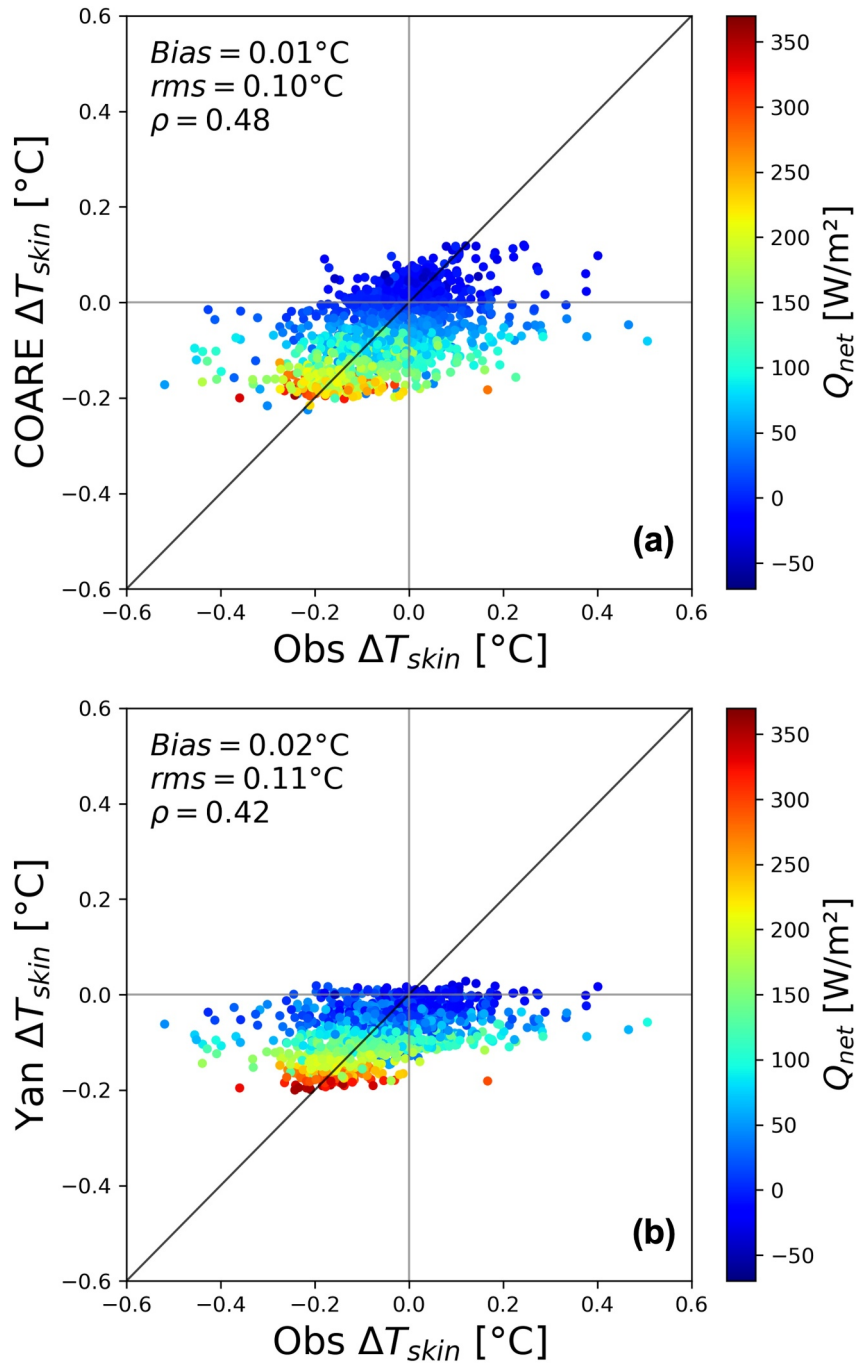

Figure 11. Scatter plots of the (a) COARE ΔT_{skin} and (b) Yan et al. (2024) ΔT_{skin} vs. observed ΔT_{skin}. The scatter plots are color-coded by the net heat flux, showing clear stratification of ΔT_{skin} with Q_{net}.

winds across the front were strong enough to prevent any warming. Thus, it is reasonable to assume that wind shear was driving the turbulent mixing on the cool side. On the warm side, the high winds enhanced evaporation and the mixing was driven by forced convection (both buoyancy and wind shear). This can be interpreted as evidence of the ocean forcing the atmosphere through the heat fluxes out of the ocean. Further supporting evidence includes the positive correlation between the *SST* perturbations across the front and the heat flux, and the ΔT_{skin} response, respectively. The winds, on the other hand, were positively correlated with the SST_{skin} only on the warm side of the front and negatively correlated on the cool side. This negative correlation can be interpreted as evidence of the atmosphere driving the ocean response on the cool side of the front. In the end, the feedback

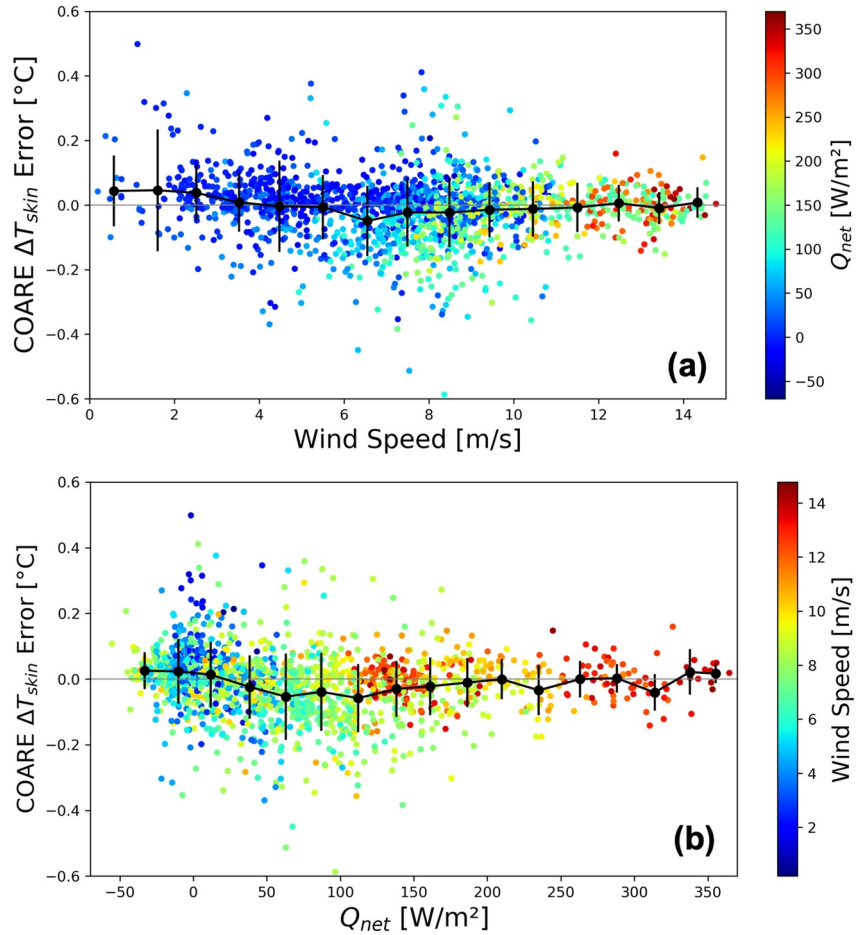

Figure 12. Dependence of the error in COARE ΔT_{skin} minus the observed ΔT_{skin} as a function of (a) wind speed and (b) net heat flux. The binned error bar curves in panels (a, b) show no significant dependence of the errors in the COARE ΔT_{skin} with either of the variables.

between both the ocean response and the atmosphere response appears to reduce the SST gradient, driven by the oceanic latent heat flux cooling down the water on the warmer side.

The individual measurements of ΔT_{skin} and Q_{net} for the detailed front crossing in Figure 5a and for the entire data set in Figures 8a and 8b show multiple instances of a warm skin occurring when the net heat flux is into the ocean. As noted above, these occurrences are not consistent with established understandings of the ocean surface skin layer. However, the bin-averaged curves in Figure 8 show a warm skin only when the net heat flux is downward. We suggest that a significant amount of the raw data scatter is due to the SST_{skin} uncertainty of ±0.10 K. The uncertainty is based on the rms difference between the sensor and a reference. Thus, for zero bias and a normal distribution, we would expect scatter about the mean to occur within ±0.10°C and ±0.20°C for 68% and 95% of the data, respectively. Visual inspection of the data in Figure 8 indicates that most of the scatter occurs within ±0.20°C of the bin-averaged curves. That much of the scatter is due to random measurement errors is consistent with the reduced scatter in the COARE ΔT_{skin} estimates in Figures 8c and 8d. We contend that classifying the skin layer as either cool or warm should be done using bin-averaged rather than raw data. Our result that the bin-averaged data show $\Delta T_{skin} > 0$ only for $Q_{net} < 0$ and our contention that bin-averaged data should be used when classifying the skin layer are consistent with the reporting of warm skin observations by Zhang et al. (2020) (see their Figures 4b and 7a).

The bin-averaged curves of ΔT_{skin} in Figures 8b and 8c show that the cooling generally increases with increasing heat flux and Δq. However, the observed ΔT_{skin} versus Q_{net} exhibits an almost staircase appearance where ΔT_{skin} remains constant for specific net heat flux intervals. The apparent step-like appearance of ΔT_{skin} versus Q_{net} is not

unexpected since the heat diffusion equation is a stable partial differential equation where small perturbations in the data lead to small variations in temperature, but at a later time as a result of the maximum principle. This delayed response is why the time evolution of the heat equation gives rise to a step response. In contrast, the COARE ΔT_{skin} versus Q_{net} dependence in Figure 8e predicts a smooth, monotonically decreasing function for positive fluxes between 0 and 275 W m^{-2}. For $Q_{net} > 275$ W m^{-2}, ΔT_{skin} appears to level off to a value of -0.18°C compared to the observations that reach a level of $\Delta T_{ski} = -0.2$°C for $Q_{net} > 275$ W m^{-2}. The apparent improved agreement between ΔT_{skin} and Δq demonstrates the general dominance of Q_E (except on the cool side of the front as noted above) and could also reflect the impact of small uncertainties in the heat flux computations and the input environmental measurements.

Our observations showed a typical net heat flux change of $Q_{net} \sim 120$–140 W m^{-2} across transects up to 25 km in length in association with a change across the thermal front of $\Delta SST_{skin} \sim 4$°C. These strong SST variations are significantly larger than previously reported. Shao et al. (2019) reported on ship-based measurements across submesoscale frontal features in the Gulf of Mexico. The cross-front temperature differences observed were approximately 1°C under moderate wind speed conditions of 7–9 m s^{-1} and sea-air temperature difference of ∼5°C. Under these conditions, they reported a maximum increase in latent heat flux from the cold to warm side of 70 W m^{-2} and a maximum increase in wind stress of 67%. Most recently, Iyer et al. (2022) made flux observations in tropical trade winds near Barbados using observations from a ship, SWIFT drifters, and Wave Gliders. Typical conditions were similar to those reported by Shao et al. (2019) of 1°C across the front, wind speed of 6–8 m s^{-1}, and a somewhat smaller sea-air temperature difference 0.6°C–1.6°C. They reported ΔSST of 0.7°C across 10–100 km variations of 50 W m^{-2} in ΔQ_E and 10 W m^{-2} in ΔQ_H.

The results comparing the COARE prediction to observations in Figures 9 and 10 are consistent with a tendency for the COARE cool skin model to underestimate the range in the magnitude of ΔT_{cool}. An underestimate of SST_{skin} could also result if the $SST_{subskin}$ were underestimated (relative to SST_{depth}) in the presence of diurnal warming. The underestimation of SST_{skin} does tend to occur more frequently when there is warming of the skin layer, which could also suggest the potential for warming of a deeper surface layer. Inclusion of the COARE warm layer model to explicitly adjust SST_{depth} to $SST_{subskin}$ under diurnal warming, however, did not significantly change the results.

Although the comparison of the COARE ΔT_{skin} versus observed ΔT_{skin} in Figure 11 showed good agreement, the correlation coefficient was $\rho = 0.48$. This relatively low correlation is in fact a slight improvement to previous ΔT_{skin} intercomparisons (e.g., Castro et al., 2003), perhaps due to the better performance of the current generation of shipboard infrared radiometers. The low correlation, however, points to the limitations of existing ΔT_{skin} parameterizations, since these still fail to account for additional mechanisms contributing to the stratification of the skin layer. The correlation excluding daytime observations with wind speeds less than 6 m s^{-1} (not shown), only improves the correlation by 0.02. This result confirms that the low correlations are not the result of daytime data contaminated with diurnal warming, but likely from incomplete physics in the ΔT_{skin} parameterizations. Additional refinements to the COARE cool skin algorithm are being implemented at NOAA. While the results in Figure 8c supported the potential for simplified estimation of ΔT_{skin} from Δq, the performance of the Yan et al. (2024) model was slightly poorer than for the COARE model from which it was derived. Further comprehensive error analyses of different cool skin models are the subject of future work.

The results show the expected tendency for the flux difference to approach zero as ΔT_{skin} approaches zero. The tendency for the computed flux to be greater with inclusion of the skin layer model in the presence of a cool skin and smaller in the presence of a warm skin suggests a tendency for the COARE fluxes computed using the skin layer model to overestimate the range of the heat flux relative to those computed directly from the observed skin temperature. An overestimation of the range of the flux is consistent with underestimation of ΔT_{skin} by the COARE model. If the estimated skin temperature is too large in the presence of skin layer cooling, the flux would be enhanced due to a larger difference from the corresponding air temperature. Similarly, if the skin temperature is too low, the flux is reduced.

Overall, however, the differences in the computed net heat flux resulting from introduction of the skin layer model are small enough to be within acceptable limits for closing the heat budget. As long as ΔT_{skin} is within ±0.3°C, the net flux is within the ±10 Wm^{-2}. Note that, while $\Delta T_{skin} = -0.3$°C is at the high end of the ΔT_{skin} range and not unusual for low to moderate winds, $\Delta T_{skin} = +0.3$°C, however, is at the bottom of the ΔT_{DWL} range (some authors choose to report ΔT_{DWL} only when in excess of 0.5°C) and, warming can, in fact, reach values near 3–5°C under

extreme conditions. Due to the lack of significant diurnal warming during IOP-1, it was not possible to properly evaluate the general impact of diurnal warming on net heat flux bulk predictions with COARE. Finally, an independent computation of the net heat flux directly from SST_{depth} without any consideration of the skin layer also indicated an overall rms net heat flux difference of 4.5 W m^{-2} (not shown) from that computed explicitly from the observed skin temperature. Neglecting the presence of ΔT_{skin} during IOP-1, thus, introduces an additional error of 1.5 W m^{-2} on the COARE Q_{net} estimate, if computed directly from SST_{depth}. This is still below the Fairall, Bradley, Godfrey, et al. (1996) heat flux accuracy requirement of 10 W m^{-2}.

5. Conclusions

The *SST* front repeatedly sampled during the S-MODE IOP1 campaign consisted of a near-neutral surface layer on the cool side (absence of convection and stratification) associated with strong winds and an unstable surface layer on the warm side, typical of nighttime oceanic conditions. This resulted in the presence of a cool skin layer on the warm side of the front only. Additionally, there was positive correlation and strong modulation in the net heat flux response to changes in the air-sea temperature difference across the front. The winds, on the other hand, were positively correlated with the SST_{skin} only on the warm side of the front and negatively correlated on the cool side. This suggests that the wind played both a destratifying role on the cool side through enhanced turbulent mixing and a stratifying role at the warm side through enhanced evaporation. The latter is indicative of the ocean forcing the atmosphere on the warm side of the front through heat flux losses from the ocean to the atmosphere, mainly, through the latent heat flux. At the same time, the atmosphere impacted the ocean on the cool side through wind shear. Wind speeds ∼8 m s$^{-1,}$ and a north-northwest direction remained unchanged for most of the experiment, which might explain the persistence of the SST front.

An analysis of the *SST* front spatial variability with distance showed that the frontal transects had gradient amplitudes between 0.1 and 0.6°C km^{-1} across horizontal distances in the range of 2–30 km, with most of the frontal crossings covering distances between 5 and 25 km. The decay of the thermal front amplitude with distance appeared to be exponential for sufficiently large *SST* gradient and where there was a change in sign of the thermal stability across the front. This indicated the presence of statistical self-similarity, or scaling invariance between ∇SST_{skin} and distance across the front. The scale invariance hypothesis was proven to hold for submesoscale fronts that obeys the power law function: $\nabla SST_{skin} \sim l^{-5/7}$, valid for a range of horizontal length scales of approximately 4–20 km.

The large number of transects throughout the duration of the campaign enabled an examination of the modulation of the net heat flux, wind speed and ΔT_{skin}, in response to the changes in SST_{skin} across the front. The main findings are:

1. The response of Q_{net} to changes in front strength ΔSST_{skin} was highly correlated and occurred in phase, suggesting a strong, positive and synchronous relationship between the two. This was further confirmation for a causal or predictive relationship between the cross-frontal modulation of Q_{net} to changes in SST_{skin}. The strong, in-phase correlation appears to hold for fronts with ΔSST_{skin} up to ∼4°C in peak amplitude. For an increase in front strength between 1°C and 4°C, the differential increase in ΔQ_{net} between opposite ends of the front varied between ∼25 and ∼140 W m^{-2}.
2. The response of the wind speed to changes in front strength showed a slight tendency for the amplitude of the wind variability across the front to increase with front strength, though there was no clear functional dependence of the wind speed response to front strength. The amplitude of the increase appeared to be influenced by the stability conditions. Where the stability did not change, the ΔU modulation varied between ∼2.5 and 3.0 m s^{-1}. For conditions when there was a change in stability across the front, the wind modulation with front strength varied between ∼3.0 and 4.0 m s^{-1}.
3. The $\Delta(\Delta T_{skin})$ modulation with ΔSST_{skin} showed a tendency to increase with front strength. For an increase in front strength between 1 and 5°C, the resulting increase in $\Delta(\Delta T_{skin})$ varied between ∼0.1 and 0.2°C and ∼0.3–0.4°C, respectively. Significant changes in ΔT_{skin} occurred in the absence of notable changes in the wind speed, suggesting the skin layer stratification is the result of the combined effect of the sources of turbulence that dominate at a given time.

Through sensitivity analyses of the COARE v3.6 bulk flux algorithm using the radiometric SST_{skin} and sea snake SST_{depth} measurements, we further demonstrated several aspects regarding the accuracy of estimates of ΔT_{skin} and

Q_{net} under conditions occurring during S-MODE IOP-1. Given the prevailing strong winds (>7 m s^{-1}) suppressing diurnal warming, SST_{depth} measurements from the sea snake were representative of the $SST_{subskin}$ and enabled reliable estimates of ΔT_{skin}. Application of the COARE skin layer model using SST_{depth} within COARE yielded net heat flux estimates within 3 W m^{-2} of that derived directly from the observed skin temperature. Fully neglecting the skin layer resulted in heat flux differences of only 4.5 W m^{-2}. These differences are small relative to typically stated accuracy requirements of ∼10 W m^{-2}, under the sampled conditions. We conclude that the heat flux could be reliably estimated without direct measurement of the SST_{skin} and that the SST_{depth} alone provided sufficient accuracy to close the heat budget. While the COARE ΔT_{skin} estimates reproduced the observations with a rms difference of 0.11°C, the correlation of 0.48 was relatively low. The poor correlation might be due to the COARE ΔT_{skin} algorithm neglecting some physical mechanisms of turbulent mixing influencing the observed ΔT_{skin}, such as in the surface renewal ΔT_{skin} model of Castro et al. (2003) that includes additional time scales for wave related processes. A ΔT_{skin} parameterization of the diffusive sublayer should potentially include submesoscale processes related to mixed layer eddies such as instabilities introduced by eddy-induced overturning. A simplified ΔT_{skin} parameterization based on the humidity difference, as in (3), was more successful in accurately reproducing the observations than one based on wind speed, as in (2), due presumably to the large variations of the heat flux across the strong thermal front during S-MODE.

Appendix A: Wind Speed and Direction Derivation

Examination of the ASIMET wind vane and compass output (not shown) indicated that the vane's orientation occasionally froze, which coincided with anomalous jumps in the compass orientation. The WS-501 wind measurements, on the other hand, suffered from occasional shadowing from the ship's superstructure. Derivation of the wind speed and direction was accomplished using common vector analysis techniques to correct for the ship's motion through a combination of the relative measurements from the two weather systems (i.e., relative wind speed vectors from ASIMET and the apparent wind direction from the WS-501). Prior to the ship motion correction, very low ASIMET apparent wind speeds (<1.5 m s^{-1}) were first interpolated using a spline of order 3 and then smoothed via a Savitzky-Golay (SG) filter (Savitzky & Golay, 1964). This filter reduces noise by fitting polynomials to adjacent data points using linear least squares, while preserving the overall shape of the signal. The SG filter used a polynomial of order 3 and had a window size of 13 min. The winds estimated in this manner compared favorably with independent estimates from NWP reanalyzesA and saildrones.

Appendix B: Use of Sea Snake SST_{depth} Measurement for $SST_{subskin}$

To evaluate the applicability of the sea snake to $SST_{subskin}$ in the daytime during S-MODE IOP-1, we examined the predicted warming above a depth of 5-cm using the turbulent mixed layer model of Kantha and Clayson (2004) as implemented by Wick et al. (2024), KCW ΔT_{DWL}, as well as the COARE warm layer model. The simulations were forced by the measured wind speed and the COARE-derived heat flux estimates. The results of the Wick et al. (2024) model from DOY 287–300 (October 14–26) in Figure B1 show that diurnal warming at all depths was minimal. There was negligible warming predicted between the 5-cm depth and the subskin and a warming of less than 0.3 K is predicted at 5-cm depth relative to a deeper depth of 5 m during the period between DOY 288–292 (October 15–19), when the wind speeds dropped to ∼ 4 m s^{-1} and below. The earlier period on DOY 284 (October 11) was treated separately due to a data gap, associated with an unplanned port visit between DOY 285–286 (October 12–13), but the results (not shown) had no significant diurnal warming. The results from the COARE warm layer model (not shown) also suggested that the warming between the 5-cm depth and the subskin did not exceed 0.04 K. As a result, we conclude that the sea snake does indeed provide a good estimate of $SST_{subskin}$ during IOP-1, even during the daytime.

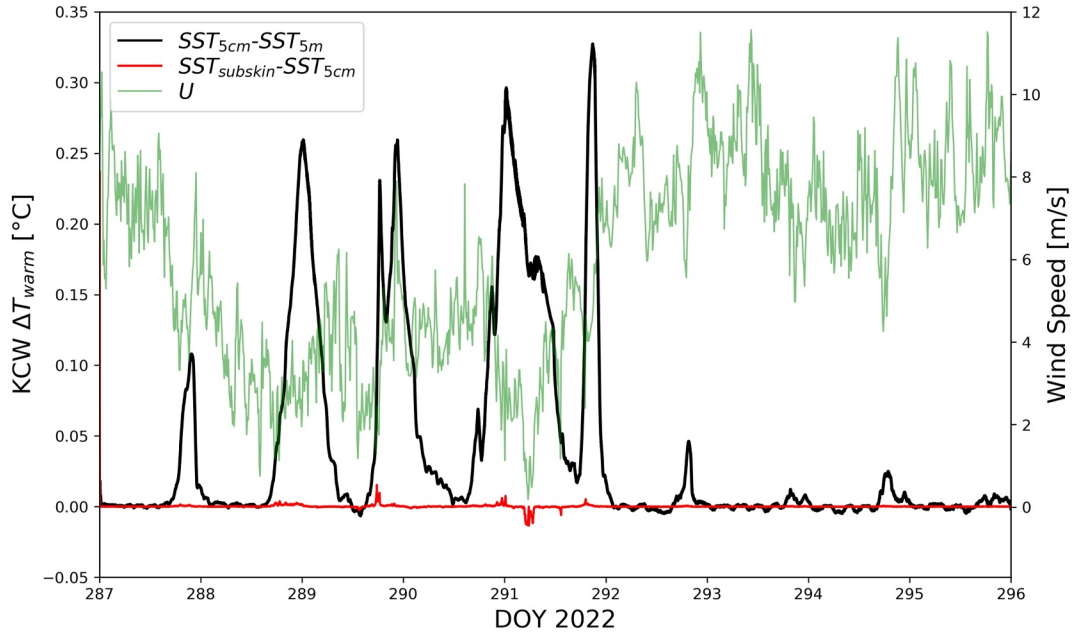

Figure B1. Estimated warming from the 1-D KCW turbulence closure model for the layer between the bottom of the skin layer (the $SST_{subskin}$) and the nominal depth (~5 cm below the surface) of the sea snake SST (SST_{5cm}) in red, and between the depth of the sea snake and the SST_{depth} at 5 m-depth (SST_{5m}) in black. The wind speed is shown in green for comparison.

Conflict of Interest

The authors declare no conflicts of interest relevant to this study.

Data Availability Statement

Observational data used in this work is archived at the S-MODE data repository at the NASA/JPL PO. DAAC (https://podaac.jpl.nasa.gov/S-MODE). The COARE bulk flux v3.6 algorithm used in the analyses was downloaded from the NOAA PSL Github at https://github.com/NOAA-PSL/COARE-algorithm. Jupyter notebooks with analysis codes can be accessed at https://github.com/M0nstrico/S-MODE.

Acknowledgments

This work is a contribution to the S-MODE project, an ESV-3 investigation awarded under NASA Research Announcement NNH17ZDA001N-EVS3. Participation of ATJ was supported by NSF award 2022750 to the University of Washington. SLC was supported by NASA S-MODE supplemental award 80NSSC24K0489 to the University of Colorado and a sub-award to the NSF award granted to the University of Washington (ATJ PI). GAW was supported by internal funding at the NOAA Physical Sciences Laboratory. We thank E. Thompson, NOAA Physical Science Laboratory, for the loan of ROSR s/n 9. The constructive comments of four anonymous reviewers are appreciated.

References

Castro, S. L., Wick, G. A., & Emery, W. J. (2003). Further refinements to models for the bulk-skin sea surface temperature difference. *Journal of Geophysical Research*, *108*(12). https://doi.org/10.1029/2002JC001641

Chelton, D. B., Schlax, M. G., & Samelson, R. M. (2007). Summertime coupling between sea surface temperature and wind stress in the California current system. *Journal of Physical Oceanography*, *37*(3), 495–517. https://doi.org/10.1175/jpo3025.1

Donlon, C. J., Minnett, P. J., Gentemann, C., Nightingale, T. J., Barton, I. J., Ward, B., & Murray, M. J. (2002). Towards improved validation of satellite sea surface skin temperature measurements for climate research. *Journal of Climate*, *15*(4), 353–369. https://doi.org/10.1175/1520-0442(2002)015<0353:tivoss>2.0.co;2

Donlon, C. J., Nightingale, T. J., Sheasby, T., Turner, J., Robinson, I. S., & Emery, W. J. (1999). Implications of the oceanic thermal skin temperature deviation at high wind speed. *Geophysical Research Letters*, *26*(16), 2505–2508. https://doi.org/10.1029/1999gl900547

Donlon, C. J., Robinson, I. S., Reynolds, R. M., Wimmer, W., Fisher, G., Edwards, R., & Nightingale, T. J. (2008). An Infrared Sea surface temperature Autonomous Radiometer (ISAR) for deployment aboard Volunteer Observing Ships (VOS). *Journal of Atmospheric and Oceanic Technology*, *25*(1), 93–113. https://doi.org/10.1175/2007JTECHO505.1

Edson, J. B., Jampana, V., Weller, R. A., Bigorre, S., Plueddemann, A. J., Fairall, C. W., et al. (2013). On the exchange of momentum over the open ocean. *Journal of Physical Oceanography*, *43*(8), 1589–1610. https://doi.org/10.1175/jpo-d-12-0173.1

Fairall, C. W., Bradley, E. F., Godfrey, J. S., Wick, G. A., Edson, J. B., & Young, G. S. (1996). Cool-skin and warm-layer effects on sea surface temperature. *Journal of Geophysical Research*, *101*(C1), 1295–1308. https://doi.org/10.1029/95jc03190

Fairall, C. W., Bradley, E. F., Hare, J. E., Grachev, A. A., & Edson, J. B. (2003). Bulk parameterization of air-sea fluxes: Updates and verification for the COARE algorithm. *Journal of Climate*, *16*, 571–591. https://doi.org/10.1175/1520-04422003016<0571:BPOASF<2.0.CO;2

Fairall, C. W., Bradley, E. F., Rogers, D. P., Edson, J. B., & Young, G. S. (1996). Bulk parameterization of air-sea fluxes for TOGA-COARE. *Journal of Geophysical Research*, *101*(C2), 3747–3764. https://doi.org/10.1029/95jc03205

Fairall, C. W., White, A. B., Edson, J. B., & Hare, J. E. (1997). Integrated shipboard measurements of the marine boundary layer. *Journal of Atmospheric and Oceanic Technology*, *14*(3), 338–359. https://doi.org/10.1175/1520-0426(1997)014<0338:ismotm>2.0.co;2

Fox-Kemper, B., Ferrari, R., & Hallberg, R. (2008). Parameterization of mixed layer eddies. Part I: Theory and diagnosis. *Journal of Physical Oceanography*, *38*(6), 1145–1165. https://doi.org/10.1175/2007jpo3792.1

Gupta, V. K., Castro, S. L., & Over, T. (1996). On scaling exponents of spatial peak flows from rainfall and river network geometry. *Journal of Hydrology*, *187*(1–2), 81–104. https://doi.org/10.1016/S0022-1694(96)03088-0

Hayes, S. P., McPhaden, M. J., & Wallace, J. M. (1989). The influence of sea-surface temperature on surface wind in the Eastern Equatorial Pacific: Weekly to monthly variability. *Journal of Climate*, *2*(12), 1500–1506. https://doi.org/10.1175/1520-0442(1989)002<1500:tiosst>2.0.co;2

Hosegood, P., Gregg, M., & Alford, M. (2006). Sub-mesoscale lateral density structure in the oceanic surface mixed layer. *Geophysical Research Letters*, *33*(22), L22604. https://doi.org/10.1029/2006GL026797

Iyer, S., Drushka, K., Thompson, E. J., & Thomson, J. (2022). Small-scale spatial variations of air-sea heat, moisture, and buoyancy fluxes in the tropical trade winds. *Journal of Geophysical Research-Oceans*, *127*(10), e2022JC018972. https://doi.org/10.1029/2022JC018972

Jessup, A. T. (2025). The InfraRed instrument for sea surface temperature (IRISS): An innovative and simplified design for measuring Ocean surface skin temperature. *Journal of Atmospheric and Oceanic Technology*. https://doi.org/10.1175/JTECH-D-24-0147.1

Jessup, A. T., Asher, W. E., Atmane, M., Phadnis, K., Zappa, C. J., & Loewen, M. R. (2009). Evidence for complete and partial surface renewal at an air-water interface. *Geophysical Research Letters*, *36*(16). https://doi.org/10.1029/2009gl038986

Jia, C., & Minnett, P. J. (2023). Ocean warm skin signals observed by Saildrone at high latitudes. *Geophysical Research Letters*, *50*(7), e2022GL102384. https://doi.org/10.1029/2022gl102384

Jia, C., Minnett, P. J., Szczodrak, M., & Izaguirre, M. (2023). High latitude sea surface temperatures derived from Saildrone infrared measurements. *IEEE Transactions on Geoscience and Remote Sensing*, *6*.

Kantha, L. H., & Clayson, C. A. (2004). On the effect of surface gravity waves on mixing in the oceanic mixed layer. *Ocean Modelling*, *6*(2), 101–124. https://doi.org/10.1016/s1463-5003(02)00062-8

Katsaros, K. B. (1980). The aqueous thermal boundary layer. *Boundary-Layer Meteorology*, *18*(1), 107–127. https://doi.org/10.1007/bf00117914

Kudryavtsev, V. N., & Luchnik, G. L. (1979). On the thermal state of the cool skin. *Proceedings, marine hydrophysical institute* (Vol. 3, pp. 105–112).

Kudryavtsev, V. N., & Soloviev, A. (1981). The thermal state of the ocean surface, Izvestiya. *Atmospheric and Ocean Physics*, *17*(10), 788–792. https://nsuworks.nova.edu/occ_facarticles/686

Kudryavtsev, V. N., & Soloviev, A. V. (1985). On the parameterization of the cold film on the ocean surface, Izvestia. *Atmospheric and Ocean Physics*, *21*, 177–183.

Liu, W. T., & Businger, J. A. (1975). Temperature profile in the molecular sublayer near the interface of a fluid in turbulent motion. *Geophysical Research Letters*, *2*(9), 403–404. https://doi.org/10.1029/gl002i009p00403

Mahadevan, A., Tandon, A., & Ferrari, R. (2010). Rapid changes in mixed layer stratification driven by submesoscale instabilities and winds. *Journal of Geophysical Research*, *115*(C3). https://doi.org/10.1029/2008JC005203

Minnett, P. J., Smith, M., & Ward, B. (2011). Measurements of the oceanic thermal skin. *Deep-Sea Research II*, *58*(6), 861–868. https://doi.org/10.1016/j.dsr2.2010.10.024

Moum, J. N., & Smith, W. D. (2019). Upper Ocean mixing. In J. K. Cochran, J. H. Bokuniewicz, & L. P. Yager (Eds.), *Encyclopedia of Ocean Sciences* (3rd ed.), (Vol. 1, pp. 71–79). Elsevier. https://osu-wams-blogs-uploads.s3.amazonaws.com/blogs.dir/4122/files/2021/01/11573.pdf

O'Neill, L. W., Chelton, D. B., & Esbensen, S. K. (2010). The effects of *SST*-induced surface wind speed and direction gradients on midlatitude surface vorticity and divergence. *Journal of Climate*, *23*, 225–281.

O'Neill, L. W., Chelton, D. B., & Esbensen, S. K. (2012). Covariability of surface wind and stress response to sea surface temperature fronts. *Journal of Climate*, *25*(17), 5916–5942. https://doi.org/10.1175/JCLI-D-11-00230.1

Park, K.-A., Cornillon, P., & Codiga, D. L. (2006). Modification of surface winds near ocean fronts: Effects of Gulf Stream rings on scatterometer (QuikSCAT, NSCAT) wind observations. *Journal of Geophysical Research*, *111*(C3), C03021. https://doi.org/10.1029/2005JC003016

Price, J. F., Weller, R. A., & Pinkel, R. (1986). Diurnal cycling: Observations and models of the upper ocean response to diurnal heating, cooling, and wind mixing. *Journal of Geophysical Research*, *91*(C7), 8411–8427. https://doi.org/10.1029/jc091ic07p08411

Robinson, I. S., Wells, N. C., & Charnock, H. (1984). The sea surface thermal boundary layer and its relevance to the measurement of sea surface temperature by airborne and spaceborne radiometers. *International Journal of Remote Sensing*, *5*(1), 19–45. https://doi.org/10.1080/01431168408948787

Saunders, P. M. (1967). The temperature at the ocean-air interface. *Journal of the Atmospheric Sciences*, *24*(3), 269–273. https://doi.org/10.1175/1520-0469(1967)024<0269:ttatoa>2.0.co;2

Savitzky, A., & Golay, M. J. E. (1964). Smoothing and differentiation of data by simplified least squares procedures. *Analytical Chemistry*, *36*(8), 1627–1639. https://doi.org/10.1021/ac60214a047

Shao, M., Ortiz-Suslow, D. G., Haus, B. K., Lund, B., Williams, N. J., Özgökmen, T. M., et al. (2019). The variability of winds and fluxes observed near submesoscale fronts. *Journal of Geophysical Research-Oceans*, *124*(11), 7756–7780. https://doi.org/10.1029/2019JC015236

Small, R. J., de Szoeke, S. P., Xie, S. P., O'Neill, L., Seo, H., Song, Q., et al. (2008). Air-sea interaction over ocean fronts and eddies. *Dynamics of Atmospheres and Oceans*, *45*(3–4), 274–319. https://doi.org/10.1016/jdynatmoce.200801.001

Sorbjan, Z. (2010). Gradient-based scales and similarity laws in the stable boundary layer. *Quarterly Journal of the Royal Meteorological Society*, *136*(650), 1243–1254. https://doi.org/10.1002/qj.638

Thomas, L. N., & Ferrari, R. (2008). Friction, frontogenesis, and the stratification of the surface mixed layer. *Journal of Physical Oceanography*, *38*(11), 2501–2518. https://doi.org/10.1175/2008jpo3797.1

Wick, G. A., Castro, S. L., Harris, A., & Mittaz, J. (2024). Evaluation of modeled diurnal warming estimates for application to producing sea surface temperature analyses. *Earth and Space Science*, *11*(9), e2024EA003619. https://doi.org/10.1029/2024EA003619

Wick, G. A., Emery, W. J., Kantha, L. H., & Schluessel, P. (1996). The behavior of the bulk-skin sea surface temperature difference under varying wind speed and heat flux. *Journal of Physical Oceanography*, *26*(10), 1969–1988. https://doi.org/10.1175/1520-0485(1996)026<1969:tbotbs>2.0.co;2

Wick, G. A., Ohlmann, J. C., Fairall, C. W., & Jessup, A. T. (2005). Improved oceanic cool skin corrections using a refined solar penetration model. *Journal of Physical Oceanography*, *35*(11), 1986–1996. https://doi.org/10.1175/jpo2803.1

Yan, Y., Song, X., Wang, G., & Li, X. (2024). Tropical cool-skin and warm-layer effects and their impact on surface heat fluxes. *Journal of Physical Oceanography*, *54*, 45–62. https://doi.org/10.1175/JPO-D-23-0103.s1

Yang, M., Guan, L., Qu, L., & Zhang, K. (2023). Cool skin effect and warm skin phenomenon observed by shipboard radiometer in the Northwest Pacific. *Frontiers in Marine Science*, *10*, 1212974. https://doi.org/10.3389/fmars.2023.1212974

Zhang, H., Beggs, H., Ignatov, A., & Babanin, A. (2020). Nighttime cool skin effect observed from Infrared *SST* Autonomous Radiometer (ISAR) and depth temperatures. *Journal of Atmospheric and Oceanic Technology*, *37*(1), 33–46. https://doi.org/10.1175/JTECH-D-19-0161.1